Advanced Radiation Detection Devices: 3D Diamond Detectors and KSr_2I_5:Eu Scintillating Crystals

A Dissertation Presented for the

Doctor of Philosophy

Degree

The University of Tennessee at Knoxville

Thomas Gregory Wulz

August 2017

Abstract

First, the radiation detection charge collection properties have been determined for four diamonds with each diamond having received a fluence of 1 MeV neutron irradiation. Photoluminescence measurements were conducted at 150 K on the most irradiated diamond, revealing information about the energies of optically-active defect centers created by the neutron radiation. Then, two diamond plates, one single-crystal and the other polycrystalline, were processed using the bulk microstructural modification technique of femtosecond-pulsed laser machining. Deep reactive ion etching of the samples revealed that the laser-treated channels etch considerably faster than the surrounding diamond. Next, to create through-diamond vias (TDVs) in diamond plates, deep reactive ion etching techniques similar to those employed in the silicon industry for creating through-silicon vias were utilized. Two different diamonds, one optical-grade and one detector-grade, were used to establish a repeatable process for etching holes completely through diamond. A stainless steel foil was found to be an effective and robust etching mask for creating TDVs with an aspect ratio of 5.0. Electroplating was used to fill the TDVs with a highly conductive chromium metal. The TDVs were connected with interdigitated strips on the surface of the diamond, establishing for the first time a 3D diamond radiation detector with fully metal electrodes. Lastly, the spatial uniformity of the light emission produced by a relatively new scintillation crystal composed of potassium strontium iodide activated with europium has been explored.

Table of Contents

List of Tables

List of Figures

Chapter 1: Charge Collection Properties of Neutron Irradiated Diamond Radiation Detectors

Summary

The radiation detection charge collection properties have been determined for four single crystal, chemical vapor deposition-grown diamonds irradiated with 1 MeV neutrons. Electric field-dependent charge collection efficiency and mobility-lifetime product values were evaluated for each diamond. Using the transient current technique, the charge carrier low-field mobilities and saturation velocities were also determined. Effective carrier lifetimes were computed for both holes and electrons. Lastly, photoluminescence measurements were conducted at 150 K on the most irradiated diamond, revealing information about the energies of optically-active defect centers created by the neutron radiation.

1.1 Introduction

In high radiation environments, diamond radiation sensors have gained interest, owing to its perceived radiation hardness [1]. As the luminosity of new and existing accelerator facilities increases, silicon tracking sensors near the interaction point may no longer be sufficient for long-term operation [1]. Diamond has many unique properties that make it an attractive replacement for silicon detectors, including high electric field breakdown strength, chemical inertness, a wide band gap of 5.5 eV, high charge carrier mobility, and the highest thermal conductivity of any material [2].

The dose-dependent effects of different kinds of ionizing radiation on diamond sensors with regards to charge collection efficiency (CCE) have been reported in the literature. When

single crystal chemical vapor deposition (scCVD) diamond detectors are subjected to 25 MeV proton irradiation, they produce a larger signal from a minimum ionizing particle (MIP) than silicon detectors. However, when exposed to a high fluence of 24 GeV protons, silicon detectors produce a larger MIP signal than scCVD diamond detectors [3-5]. When exposed to a 87 MGy dose of 1.25 GeV energetic gold ions (about 4×10^{13} ions/cm^2), Pietraszko *et al* demonstrated an 80% loss of CCE in scCVD diamond detectors [6]. Bentele *et al* demonstrated a dose-dependent loss of CCE of up to 55% in scCVD diamond sensors post-neutron irradiation with fluences up to 1.1×10^{14} n/cm^2 "broad-spectrum" (between 0.5 eV and 10 MeV) neutrons [7].

When operating as a radiation detector, charge trapping in the diamond bulk or at the electrodes after irradiation leads to an effect called polarization [8-10], where a reduction in the signal amplitude over time is observed. The polarization effect is a strong function of the preparation of the diamond detector, the applied electric field, and the rate of radiation incident on the detector inducing the polarization. Different methods have been employed attempting to minimize or eliminate the polarization effects, including exposing the diamond to light [11, 12] and periodic alternating of the bias polarity [13]. Polarization observed in diamond detectors irradiated with heavy charged particles or neutrons must be better understood to mitigate its effect and increase their operational longevity for particle tracking.

1.2 Methodology

In order to study the effects of neutron irradiation on the charge collection properties of diamond, four scCVD diamonds from Element Six were irradiated at the High Flux Isotope Reactor (HFIR). The pneumatic tube used at the neutron activation analysis facility of HFIR exhibits a broad distribution of neutron energy that peaks at an energy of ~1 MeV. The physical

dimensions, respective neutron dose, and post-irradiation capacitance of each diamond are shown in Table 1.

Table 1: Element 6 scCVD diamond parameters

Sample Identifier	Plate Dimensions (mm)	Neutron Dose (n/cm^2)	Capacitance (pF)
PLT S130	4.3 x 4.3 x 0.50	5.0×10^{13}	2.70
CMS S6	5.0 x 5.0 x 0.37	5.0×10^{13}	1.92
PLT S132	4.3 x 4.3 x 0.50	5.0×10^{13}	2.85
DDL M4	4.3 x 4.3 x 0.50	4.4×10^{14}	3.00

1.2.1 Charge Collection Efficiency

The charge carrier mobilities and lifetimes of each scCVD diamond detector were evaluated post irradiation using charge CCE and transient current technique (TCT) measurements. The CCE method measures the collected charge from a diamond detector from that expected using the 13.2 eV/e-h pair (mean electron-hole pair creation energy) W-value of diamond [14, 15]. If the range of the interrogating radiation range is much smaller than the thickness of the sensor and its interaction position well-controlled, then the product of the mobility and trapping time constant ($\mu\tau$) for each charge carrier can be determined using a simplified form of Hecht's relation, as given in equation 1, where d is the detector thickness and E is the electric field across the scCVD diamond detector.

$$\boldsymbol{CCE(E) = \frac{\mu\tau E}{d}\left(1 - \exp[-\frac{d}{\mu\tau E}]\right)} \quad (1)$$

Post neutron irradiation data was collected using a 0.1 µCi ^{210}Po alpha source, an Amptek CoolFET charge sensitive preamplifier, and an ORTEC 572A amplifier and 927 ASPEC MCA. To calculate the amount of charge collected during alpha particle irradiation, the sensitivity of

the CoolFET CSA was calibrated using an Ortec 419 Precision Pulse Generator and a 1.1 picoFarad capacitor. The mean peak position was found for various applied potentials and equation 1 was used to determine $\mu\tau_e$ and $\mu\tau_h$. Before neutron irradiation, all four scCVD diamond detectors were analyzed to have 100% CCE [7]. A schematic of the signal chain is shown in Figure 1.

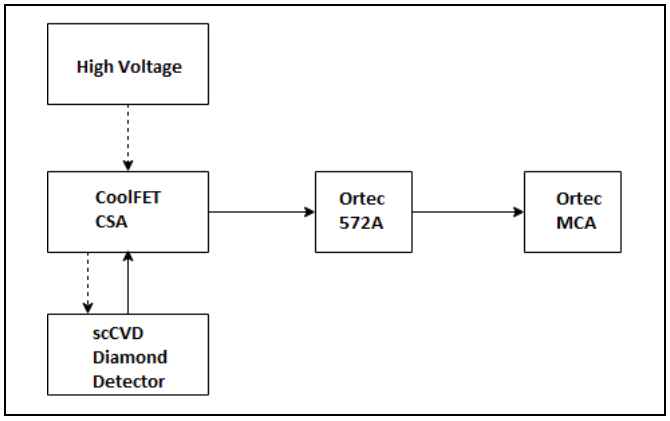

Figure 1: Diamond detector CCE signal chain

1.2.2 TCT Analysis

Direct analysis of the current pulse shape (TCT) was used to determine the transit time of electrons and holes across the scCVD diamond detectors. Individual alpha pulses were recorded and averaged using the CAEN 1423B broad band amplifier and an Agilent Infiniium, 1.5GHz, 8 GS/s oscilloscope. Figure 2 shows the schematic of the TCT data acquisition setup.

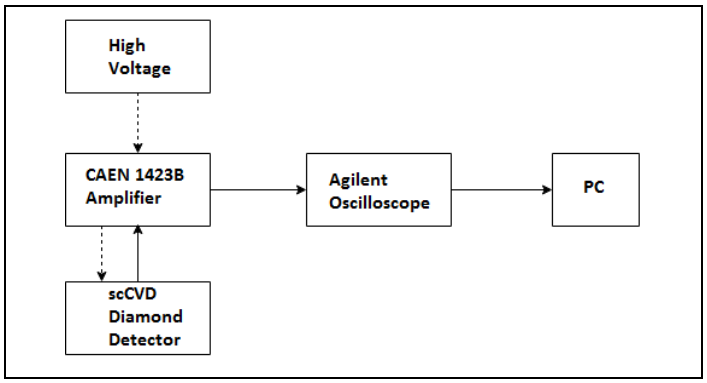

Figure 2: TCT experimental setup

The acquired averaged voltage transient, *U(t)*, for holes and electrons is converted into a transient current pulse using the relationship [16],

$$\boldsymbol{I_{m_{e,h}}(t) = \frac{1}{R_{in}A}\left[R_{in}C_d\frac{dU(t)}{dt} + U(t)\right],} \tag{2}$$

where R_{in} is the system impedance of 50 Ω, C_d is the sum of detector and stray capacitances at the input to the current-to-voltage amplifier, and A is the gain of the amplifier. The charge transit time, t_c, of the current pulses is then calculated as the full-width-at-half-maximum of the current pulse.

Since monodirectional ^{210}Po alpha particles have a range of 13 μm in diamond, as simulated via SRIM [17], all of the energy from alpha radiation exposure is deposited in the diamond near the exposed electrode. The average drift velocity of electrons and holes across the detector thickness d can then be calculated using

$$\boldsymbol{v_{dr}(E) = \frac{d}{t_c(E)}} \tag{3}$$

for electrons when the detector is positively biased and for holes when the detector is negatively biased. Charge carriers liberated by the ionizing alpha particles must traverse essentially the

entire detector thickness *d* to be collected. Consequently, a linear relationship between the drift velocity and electric field is assumed in the direct calculation of the mobility of charge carriers as

$$\boldsymbol{\mu_{0_{e,h}}} = \frac{\boldsymbol{d^2}}{\boldsymbol{Vt_c}}, \tag{4}$$

where $\mu_{0_{e,h}}$ denotes the low-field mobility for electrons or holes. In the electric field regime typically used by particle detectors (0.2-1.0 V/μm), the drift velocity of charge carriers is non-linear as a function of applied bias. The result is an over-approximation of the carrier mobility at these field strengths when using equation 4. An empirical relationship describing the non-linear behavior of the charge carrier drift velocity and applied electric field is suggested in [18] as

$$\boldsymbol{v_{dr}} = \frac{\boldsymbol{\mu_0 E}}{\boldsymbol{1+\frac{\mu_0 E}{v_s}}}, \tag{5}$$

where μ_0 is the charge carrier low-field mobility and v_s is the saturation velocity of charge carriers in the diamond bulk. Using the aforementioned relationships, the intrinsic electrical properties of four diamonds with varying neutron irradiation doses were determined.

1.2.3 Photoluminescence

In this paper, photoluminescence (PL) measurements are used to identify optically-active defect centers that act as charge trapping sites when the diamond is operated as a radiation detector, reducing its performance. PL measurements provide a quantitative analysis technique for measuring the energy of impurity trapping states in semiconductor materials. During PL, electrons from the valence band are liberated through laser excitation. The amount of energy imparted to the electrons is dependent on the energy of the excitation photons with the maximum electron energy being equal to the energy of the excitation source. Once electrons are liberated

from the valence band, atomic level defects and impurities can act as charge traps, capturing the electrons within the bandgap. When the electrons de-excite back to the valence band, a photon of energy characteristic to the charge trap can be released. These photons are detected by the PL system, which bins the intensity of photon counts as a function of photon energy.

PL measurements are often conducted at reduced temperatures to minimize secondary phonon production, which causes broadening of the PL zero-phonon line (ZPL) spectrum. In room temperature diamond PL measurements, the background luminescence signal created by non-ZPL emission often overwhelms the signal of the true ZPL. Thus, it is advantageous to conduct diamond PL measurements at reduced temperatures by cooling the sample. A graphical representation of this phenomena is shown in Figure 3.

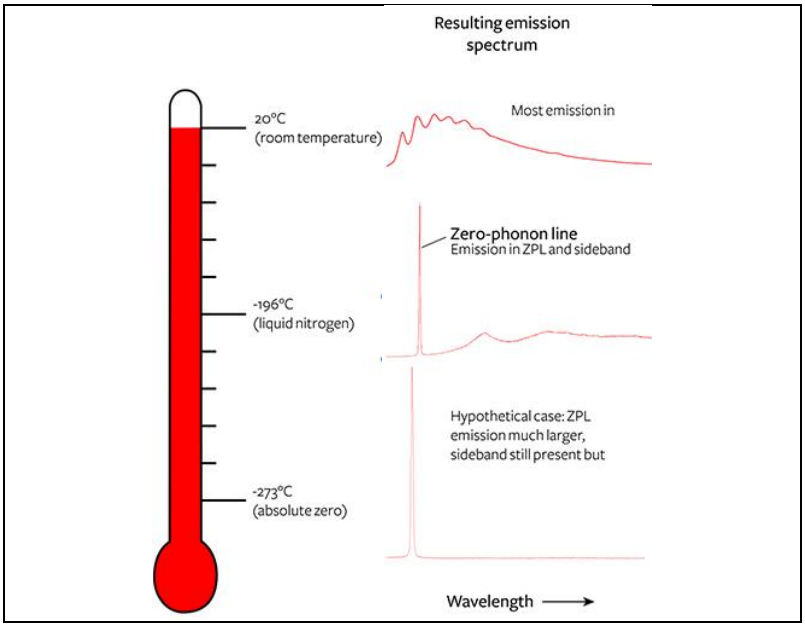

Figure 3: Theoretical effect of temperature on ZPL and sideband emission [19]

The PL technique is well suited to diamond as the material is often optically transparent, allowing for light to probe the bulk of the material. The first order Raman line at 1332 cm^{-1} also

provides a good calibration peak. Furthermore, many of the defects within synthetic and irradiated diamonds are optically active and can be revealed through proper PL measurements.

1.3 Results and Discussions

1.3.1 CCE Results

To determine the applied bias that optimizes CCE, the field strength was increased from 0.2 to 1.0 V/μm for each sample. The polarity of the applied bias was alternated after the collection of each data point in order to minimize polarization effects so that $\mu\tau_{e/h}$ could be found as accurately as possible. The electron and hole CCE curves of each sample are shown in Figure 4. It is evident that the CCE drops as a function of neutron fluence, where neutron elastic scattering events create high density cluster defects from nuclear scattering events with other nearby carbon atoms within the diamond matrix. Using a least squares fit to Equation 1, the product of the carrier mobility and lifetime was determined for each sample and is provided in Table 2.

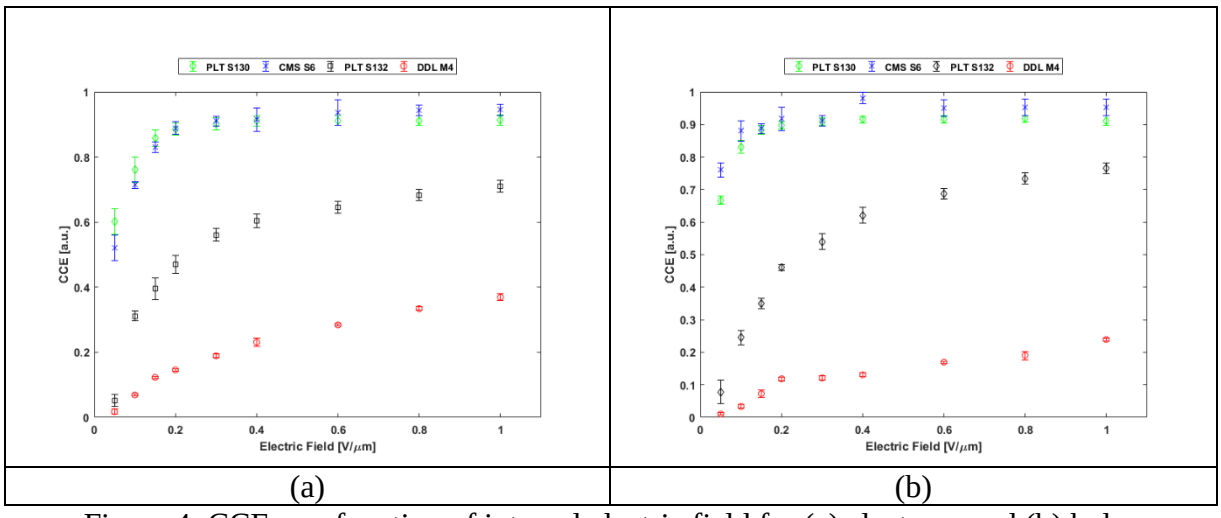

Figure 4: CCE as a function of internal electric field for (a) electrons and (b) holes

Table 2: Experimentally determined CCE and mobility-lifetime products

Sample Identifier	Post-Irradiation CCE (%)		Mobility-Lifetime Product (cm^2/V)	
	Electrons	Holes	Electrons	Holes
PLT S130	91.3 ± 1.7	91.2 ± 1.5	$(9.1 \pm 2.1) \times 10^{-5}$	$(1.5. \pm 0.3) \times 10^{-4}$
CMS S6	94.5 ± 1.7	95.2 ± 2.5	$(6.2 \pm 2.0) \times 10^{-5}$	$(1.5 \pm 0.3) \times 10^{-4}$
PLT S132	71.1 ± 1.8	76.5 ± 1.7	$(2.0 \pm 0.5) \times 10^{-5}$	$(1.4 \pm 0.1) \times 10^{-5}$
DDL M4	36.9 ± 1.0	23.9 ± 0.4	$(9.9 \pm 1.9) \times 10^{-6}$	$(7.5 \pm 1.4) \times 10^{-6}$

A qualitative measure of the neutron-induced traps in the irradiated diamond samples was found using LED exposure to sample PLT S132. The applied electric field in this study was 0.5 V/μm and sample PLT S132 was allowed to fully polarize before turning on the LED light source. The measured differential pulse height spectra from ^{210}Po alpha particles during LED illumination is provided in Figure 5. It can be seen that different effects are observed for holes and electrons across the wavelengths investigated (940nm, 640 nm, 520 nm, 465 nm, and 400 nm).

For electron collection, it was found that IR and red light were most effective at restoring $\mu\tau_e$. The response to red light restores the signal amplitude to 78% CCE. Green light yields a lower restoration of the signal amplitude than IR and red light, and this result suggests that the trap energy is near 1.94 eV. Three body excitation via phonons is likely the reason for the measured response in the IR, so the electron trap energy is likely closer to 1.94 eV than 1.32 eV because of the incomplete restoration of the CCE under IR illumination. Further, under blue light exposure, the count rate of sample PLT S132 was restored to its expected value, but at a reduced CCE. This suggests that there are at least two electron trap energies created by neutrons. The shallower trap near 1.94 eV should have a larger electron lifetime than the deeper trap around 2.67 eV, consistent with the analysis provided by Shockley and Read [20]. During blue light

illumination, it may be that the mobility is reduced or charge carrier transport takes place via hopping conduction, thereby slowing signal formation significantly, which yields the correct count rate, but not the expected signal amplitude.

For holes, the opposite trend was observed, where blue light resulted in the highest signal restoration and red and IR resulted in minimal change to the measured signal amplitude. The response of sample PLT S132 to green and blue light suggests that the trap energy for holes is between 2.39 eV and 2.67 eV.

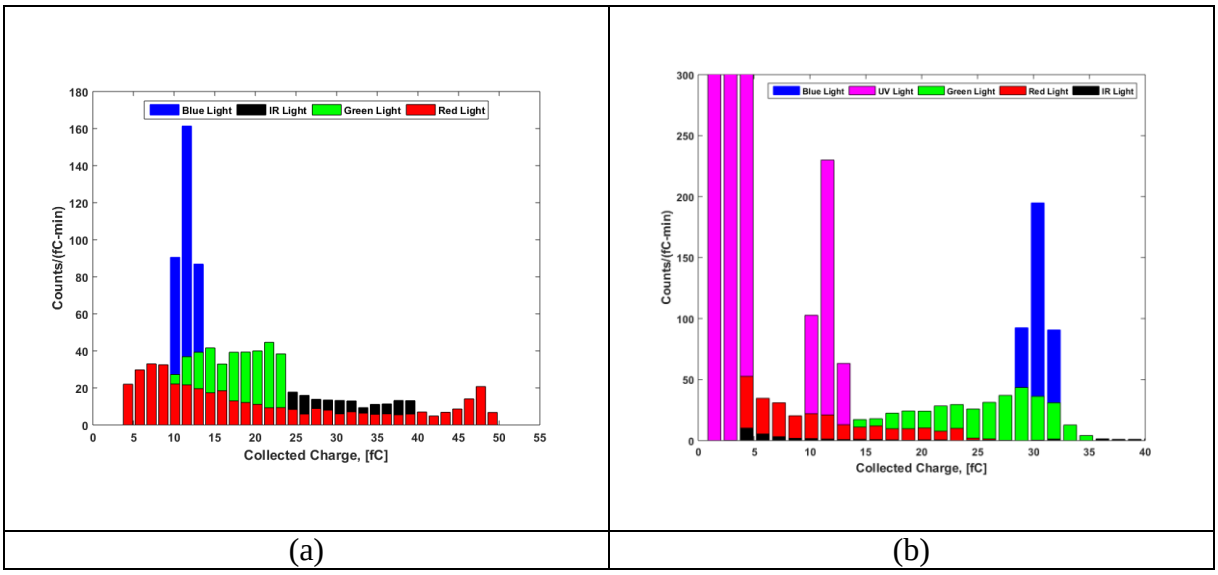

(a) (b)

Figure 5: Measured differential pulse height spectra of scCVD diamond detector PLT S132 under LED illumination for (a) electrons and (b) holes

1.3.2 TCT Results

TCT measurements were conducted to determine the drift velocity and mobility of electrons and holes in the scCVD diamond detectors at different applied electric fields. Using this data along with the CCE analysis, the lifetime of the electrons and holes in the scCVD diamond detectors can be determined. Sample TCT spectra are shown for PLT S130 in Figure 6,

where it can be seen that the drift velocity of holes exceeds that of electrons. Using equation 6, the electron and hole drift velocity as a function of applied electric field for PLT S130 is shown in Figure 7.

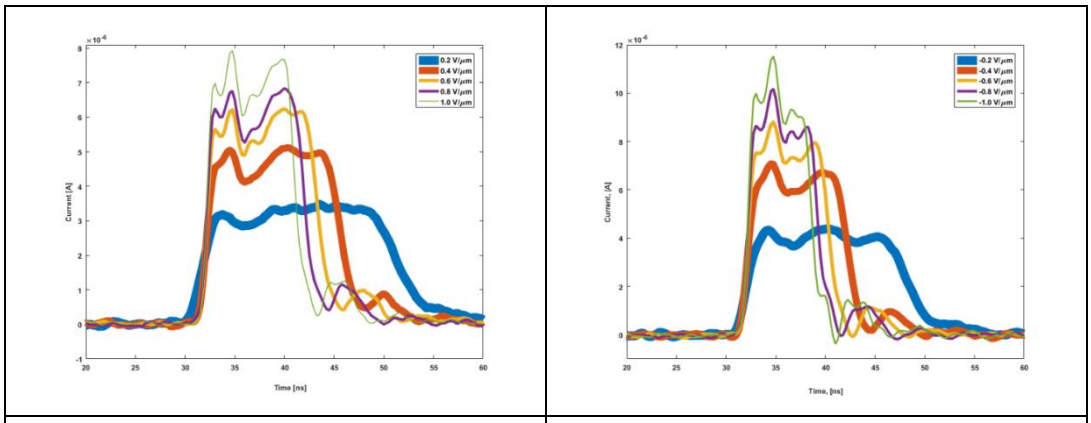

(a) (b)

Figure 6: Alpha-induced transient current profile of scCVD diamond detector PLT S130 at different applied biases for (a) electrons and (b) holes.

The electrical properties for the scCVD diamond detectors are provided in Table 3. From this data, it can be observed for the mobility of both electrons and holes increases as a function of radiation dose. Interestingly, the drift velocity remains relatively constant from an increase in the neutron dose by a factor of 2. Further, the lifetime of holes decreases at a faster rate than electrons when comparing samples PLT S130 and PLT S132. The lifetimes of both electrons and holes are severely degraded at a fluence of 10^{14} n/cm^2. For the most irradiated scCVD diamond detector, sample DDL M4, the rapid polarization did not readily allow determination of electron and hole transit times, and therefore the mobility, saturation velocity, and carrier lifetimes.

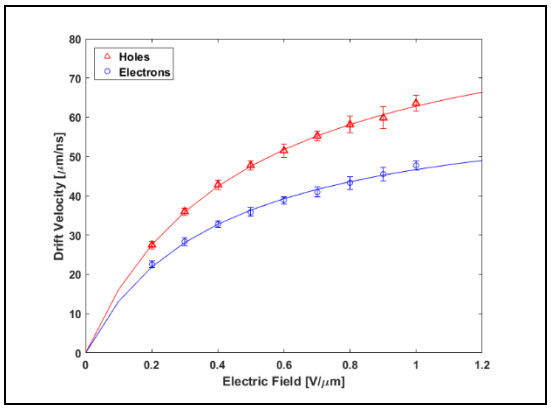

Figure 7: Charge Carrier Drift Velocities for PLT S130

Table 3: Charge carrier properties of the scCVD diamond detectors determined via TCT analysis

Sample identifier	Low-field mobility ($cm^2/V\ s$)		Saturation velocity (10^6 cm/s)		Charge carrier lifetime (ns)	
	Electrons	Holes	Electrons	Holes	Electrons	Holes
PLT S130	1649 ± 134	1960 ± 86	6.5 ± 0.3	9.2 ± 0.3	55.18	76.53
CMS S6	1862 ± 219	2114 ± 252	3.5 ± 0.1	4.1 ± 0.2	33.30	70.96
PLT S132	1971 ± 277	2269 ± 167	6.7 ± 0.5	9.5 ± 0.5	10.15	6.17
DDL M4	–	–	–	–	–	–

1.3.3 PL Results

PL measurements were conducted using a Horiba LabRAM HR Evolution confocal, Raman microscope. The system is equipped with green (532 nm) and blue (472 nm) lasers with maximum powers of 50 mW and 25 mW, respectively. Raman and PL signals are collected through a 50x microscope objective, which directs the signal to the liquid nitrogen cooled Horiba Symphony II CCD spectrometer through a 100 µm slit aperture and a grating groove density of 600 lines/mm.

Samples are mounted under vacuum in a Janis VPF-800 optical cryostat with a 0.4 L liquid nitrogen reservoir and a copper cold finger for cooling the samples. The temperature of the

samples is measured by a Type E thermocouple mounted in the copper cold finger and is readout by a Lakeshore 335 Cryogenic Temperature Controller. Fused quartz viewport windows on the cryostat allow the sample to be focused on using the confocal Raman microscope objective lenses. A flow of compressed, dry nitrogen was directed through polyethylene tubing onto the outside of the viewport windows to mitigate condensation.

PL measurements were conducted on the most irradiated sample, DDL M4, and a pristine, non-irradiated detector grade scCVD diamond, also from Element Six. This was done to provide a baseline of the expected PL peaks from an equivalent diamond that has not been irradiated by 1 MeV neutrons. The PL spectrum of both diamonds at 150 K excited by the blue laser is shown in Figure 8.

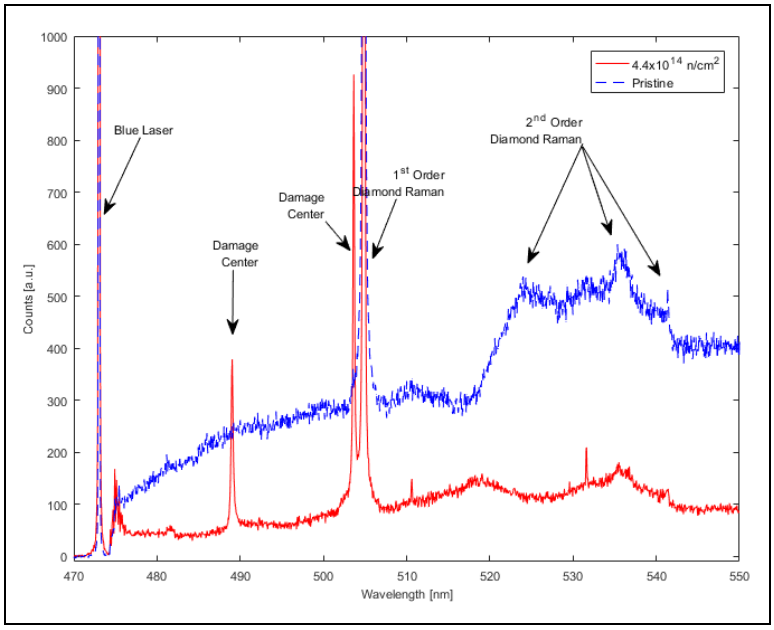

Figure 8: PL measurements with blue laser excitation at 150 K

Many features are observed in the PL spectra, including the first and second order diamond Raman peaks, as well as the blue laser excitation source. PL from optically-active defect centers is observed with a ZPL at 489.0 nm (2.54 eV) as well as at 503.7 nm (2.46 eV) when excited with the blue laser. The origin of the 489.0 nm luminescent defect center is unknown. The 503.7 nm ZPL is attributed to the S1 defect center [21]. The PL spectrum of both diamonds at 150 K excited by the green laser is shown in Figure 9.

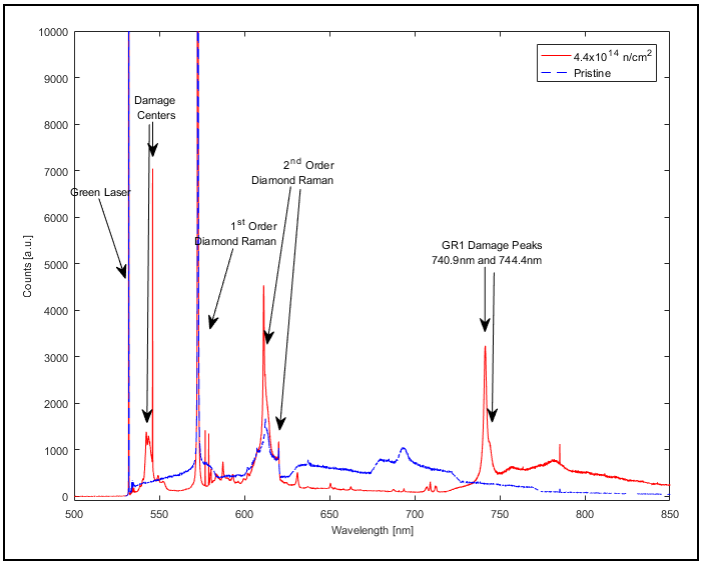

Figure 9: PL measurements with green laser excitation at 150 K

The PL spectra from green laser reveals two large defect clusters. One at the well-known GR1 damage center with convoluted ZPL peaks at 740.9 nm (1.673 eV) and 744.4 nm (1.666) eV). Other studies have demonstrated that these two peaks separate into two distinct peaks when the sample is cooled to 77 K [19]. The origin of the GR1 luminescence center is believed to be a neutral vacancy [22]. The second, deeper trapping center has an unknown origin and exhibits a ZPL peak at 546.1 nm (2.27 eV) with a sideband extending to 541 nm (2.29 eV).

1.4. Conclusions

An overall reduction in CCE was observed in all neutron-irradiated scCVD diamond detectors. Diamonds receiving a greater neutron dose displayed greater loss in CCE. The low-field mobility electrons and holes were found to potentially increase as a function of neutron dose, but the reader should be aware that this assumes that the intrinsic mobility of electrons and holes are similar across all samples, which may not be the case. The reduction in CCE is seemingly caused by decreased charge carrier lifetimes as a function of neutron dose, consistent with the understanding that the trap density increases accordingly. PL measurements were used to reveal optically active defect centers in the irradiated diamond. The predominant defect centers observed were the well-known GR1 center at 1.67 eV, the S1 center at 2.46 eV, and defect centers of unknown origins at 2.27 eV and 2.54 eV.

Chapter 2: Laser Induced Graphitization and Subsequent Dry Etching of Microchannels in Diamond

Summary

Two chemical vapor deposition-grown diamond plates, one single-crystal and the other polycrystalline, were processed using the bulk microstructural modification technique of femtosecond-pulsed laser machining. Multiple laser parameters were varied in processing the polycrystalline sample, including laser pulse frequency, pulse energy, and number of pulses per micron step size between the back and the front of the diamond, whereas a constrained set of parameters was used with the single-crystal sample. Over the range of parameters evaluated for the polycrystalline diamond, Raman analysis exhibited photoluminescence from defects created through the laser machining process but little if any graphite-like features. However, a Raman signal from graphite-like material was observed for the single-crystal diamond, from which it was determined that greater diamond to graphite-like phase conversion is obtained with a smaller number of pulses per translation step and with a higher laser pulse energy. Further, a larger number of pulses per step resulted in strong luminescence, observed during Raman investigation. Deep reactive ion etching of the samples revealed that the laser-treated channels etch considerably faster than the surrounding diamond, and that a high relative etch rate is obtained even when graphite-like features are absent from the Raman spectra. The highest relative etch rate of the laser-treated columns was 1.61 μm/min in the single-crystal sample.

2.1 Introduction

Diamond is a well-studied material, with many favorable attributes for numerous applications [2, 23-26]. In reference to the use of lasers on diamond substrates, the applications have included surface treatments [27-29], growth and ablation/etching of diamond [30-32], diffraction gratings and other elements for high power optical systems [33-35], and graphitic/conductive channel formation [29, 36-41]. The potential for directly writing conductive channels onto or into diamond for electronic applications is appealing, given the potential speed and high-dielectric constant of diamond, which are utilized in applications such as high-power switches [25]. Recent investigations, however, have demonstrated that the channel conductivity is dependent on the laser parameters [26, 40, 42, 43]. When femtosecond (fs) lasers are used, the scan speed of the laser focus through the substrate during the creation of graphitic channels is found to be a key parameter in determining the resistivity of the channels. In one recent report, a maximum conductivity of 64 S/m was obtained with a scan rate of 20 μm/s [42]. The result was correlated to the maximum ratio of the G (1500 ~ 1630 cm^{-1}) peak to the D peak (1350 cm^{-1}) in the Raman spectrum, where this ratio increases with increasing disorder. These authors also find that merely increasing the laser intensity results in non-uniform creation of graphitic centers, which they attribute to the Kerr effect (nonlinear optical self-focusing of the laser). However, when nanosecond (ns) lasers are used, the conductivity of the channels increases by an order of magnitude [43], but when used for the fabrication of 3D diamond detector devices, the diamond exhibits reduced charge collection efficiency and/or polarization (a competing internal electric field due to charge trapping) [40]. In any case, the conductivity obtained with a ns-laser is still an order of magnitude below that of crystalline graphite, and 1000 times lower than that of compressed graphite powder.

It has been indicated that for ns lasers the thermalization time of excited electrons plays a role in determining the created structure, whereas fs lasers do not allow the electrons to thermalize with the lattice during the delivery of the pulses [29]. For processing that allows thermalization with the lattice to take place, the heating of the surrounding material and the density change between diamond and graphitic-like carbon can result in mechanical stresses and cracking, and the residual pressure can be observed through Raman investigation of the stress-induced shift in the G peak [26]. Further, internal pressure can slow the progression of graphitization, even reversing it and creating nanodiamond crystallites [26, 39].

The results to date on the conductivity of graphitic channels created by either ns or fs laser machining through bulk diamond indicate that it will be very challenging to produce low-resistance channels, such as those required for fast, high-power switches or other devices. However, as demonstrated in this paper, there is the possibility to laser machine through-diamond channels that are partially graphitized, which can be etched away at a significantly faster rate than the untreated diamond to create TDVs. The TDVs may be subsequently filled with a conductive material, as is commonly done in the silicon industry [44, 45]. This paper reports the effects of various fs pulsed laser processing conditions on the level of graphitization of two chemical vapor deposition (CVD)-grown diamonds, one single-crystal (scCVD) and the other polycrystalline (pcCVD), and the deep reactive ion etching (DRIE) of the associated laser-created non-diamond carbon phase regions. DRIE, which is a form of dry chemical etching, can selectively remove sp^2 bonded over sp^3 bonded carbon to create TDVs through the diamond substrate with dimensions defined by the laser treatment process.

2.2 Methodology

The laser system used in this investigation consisted of a Ti:S oscillator (Spectra-Physics, Tsunami) with a regenerative amplifier (Coherent, RegA 9000), which provides a pulse duration of ~130 fs at 797 ± 8 nm with a maximum energy of 4 μJ. Very tight aberration-corrected focusing of the beam into the diamond was accomplished using a beam expander made of three lenses together with an aspheric lens with numerical aperture (in air) of 0.68. The beam expander was designed to deliberately introduce spherical and chromatic aberration, and two of its lenses were repositioned by motorized translators to adjust the aberration so that it pre-compensates for that produced by refraction of the beam at the surface of the diamond. The aberration pre-compensation enabled a focal spot diameter of ~1 μm to be retained as the depth of focus is translated through the diamond, although the resulting channel diameters are typically larger and depend on the number and energy of laser pulses used. During laser processing of each test channel, the initiation of a structural change within the diamond was monitored by observing diffraction of the beam from a green laser pointer, which is collinear with the fs laser beam, and following laser processing, the samples were inspected using an optical microscope.

In our studies, two diamond substrates were treated in ambient air using the fs-pulsed, aberration-corrected laser focus: Sample 1, a 500 μm thick, pcCVD diamond, and sample 2, a 300 μm thick, scCVD diamond. Sample 1 was investigated with a wide variation of the laser parameters, including pulse energy, E (0.2–4 μJ), pulse frequency (0.033–250 kHz), number of pulses per position, N (2–5000), discrete differential step height between laser treatment positions, Δz (2–12 μm), as well as continuous translation (10–100 μm/s).

Sample 2 was treated using a more constrained range of experimental parameters, guided by the results from sample 1. Two different sets of parameters were investigated, each identified by a “1” or “2” ablated into the diamond surface above the array of test points. For both arrays (4 rows × 4 columns), the laser pulsing frequency was kept constant at 2 kHz, and the step size was $\Delta z = 2$ µm. Array 1 used 10 laser pulses per z-step, while array 2 used 1000 pulses per step. In each of the arrays, the laser energies were E = 0.4, 0.8, 1.2, and 1.6 µJ from the top row to the bottom row, while the parameters were the same in each column of each array. Figure 10 shows an optical microscope image of the front surfaces of sample 1 (a) and sample 2 (b). In each case, the lateral shift between test points, obtained with a manual micrometer stage, was ~100 µm.

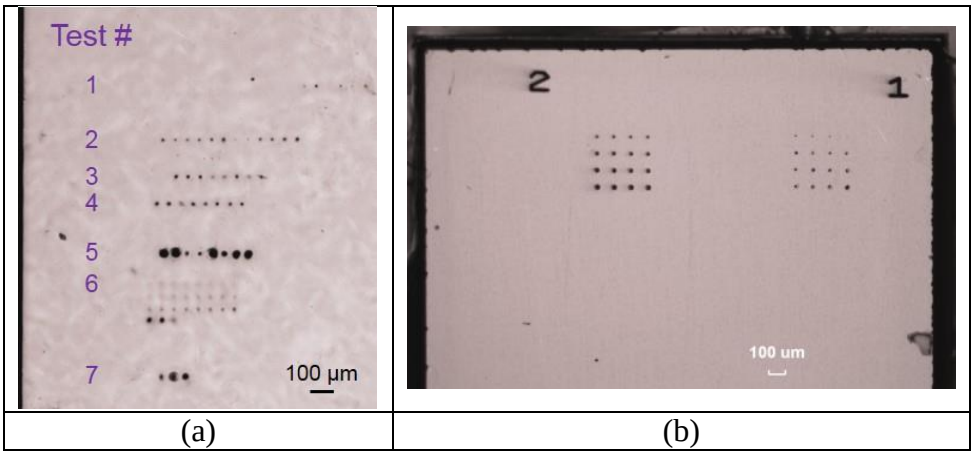

(a) (b)

Figure 10: Optical micrographs of front surface of laser-machined graphitized channels in (a) sample 1, pcCVD and (b) sample 2, scCVD

Raman spectral measurements on the created graphitic channels was acquired using a Renishaw inVia confocal Raman microscope utilizing a 633 nm excitation source with a 1 µm diameter spot size and grating with 1200 lines/mm. Correlations between the laser processing parameters and the peak intensities of diamond and graphite-like Raman signatures were determined.

DRIE of the laser-treated sample 2 was carried out in an Oxford Instruments Plasmalab100 machine capable of independently controlling the inductively-coupled plasma (ICP) coil power and radio frequency (RF) table power. During the etching process, the diamond was mounted to a four-inch silicon carrier wafer using thermally conductive Krytox^{TM} vacuum oil. The dry chemical etching of sample 2 was conducted with oxygen, an ICP coil power of 2.5 kW, and RF table power of 150 W. The surface topology of the laser processed and etched regions was characterized via sputtering chromium on the surface of the diamond followed by optical profilometry using a Veeco 8800NT white light interferometer in vertical scanning interferometry mode.

2.3 Results and Discussion

In laser machining each test channel, a structural change within the diamond was apparent from the diffraction of the collinear green laser pointer beam. However, for sample 1, it was found that, for low pulse energies (E) and number of pulses (N), features at the front surface are barely visible in the microscope image, as may be seen in Figure 11. On the other hand, for the highest pulse energy (4 μJ), a crack extending from the channel sometimes appeared at the front surface. For some conditions, the channels appeared markedly different on the front and back of the sample. Also, the direction of translation was found to have little effect on the resultant appearance of the graphitized channels, perhaps because much of the energy of each pulse converges at high angles rather than propagating along the axis and being obstructed by previously formed graphitization. Furthermore, as shown in Figure 12, for the highest pulse energy, ablation, or cratering, sometimes appeared on the front face of the sample. The extent of cratering and asymmetry of the observed features on the front and back of the sample increased as the number of laser pulses was increased. Also, the appearance of the laser-treated region of sample 1 on the back surface seemed less affected by changes in the number of pulses than that at the front. Overall, in both samples,

correlations were observed between the apparent sizes of the graphitized channels at the front and back and the laser pulse energy and number of pulses.

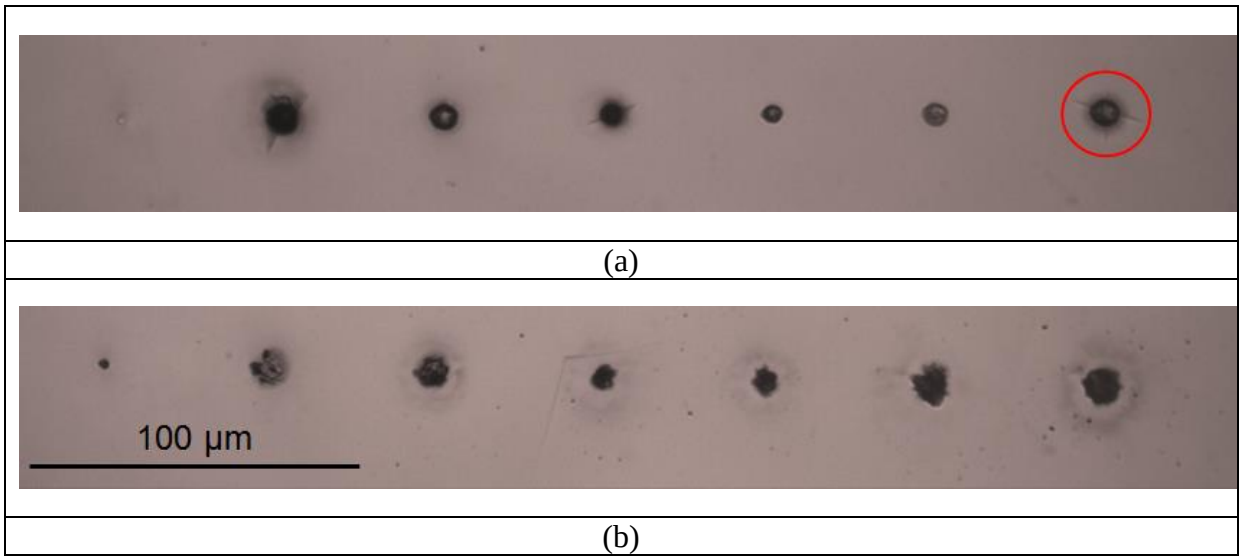

Figure 11: Microscope image of some of the resultant graphitized channels of sample 1 (pcCVD) on a) the front and b) the back surface. From left to right, the laser pulse energy is 0.4 µJ, then in pairs, 4, 2, and 4 µJ, respectively. From left, the second and fourth feature is treated from back to front and to back again, while the other channels are treated only from back to front. All treatments are conducted at 33 Hz, Δz of 3 µm, and 10 pulses per step, except for the sixth from the left, which uses 5 pulses per step. The red circle indicates one of the channels that is investigated via Raman spectroscopy, as provided in the first (blue) curve in Figure 13

For sample 1, the wider range of laser processing parameters used lead to a correspondingly more different set of Raman spectra. Sample 2 (scCVD), which was machined with a more constrained range of parameters based on results from sample 1, was found to yield a more consistent set of graphitized channels, both visually in the microscope and through Raman investigation. For sample 1, Figure 13 displays the Raman spectra of the two laser-treated channels that are identified by red circles in Figures 11 and 12. In the Raman spectrum of the identified channel in Figure 11, the characteristic 1332 cm^{-1} Raman peak for sp^3 bonded carbon is clearly apparent, and there is also an increase in Raman counts around 2250 cm^{-1}

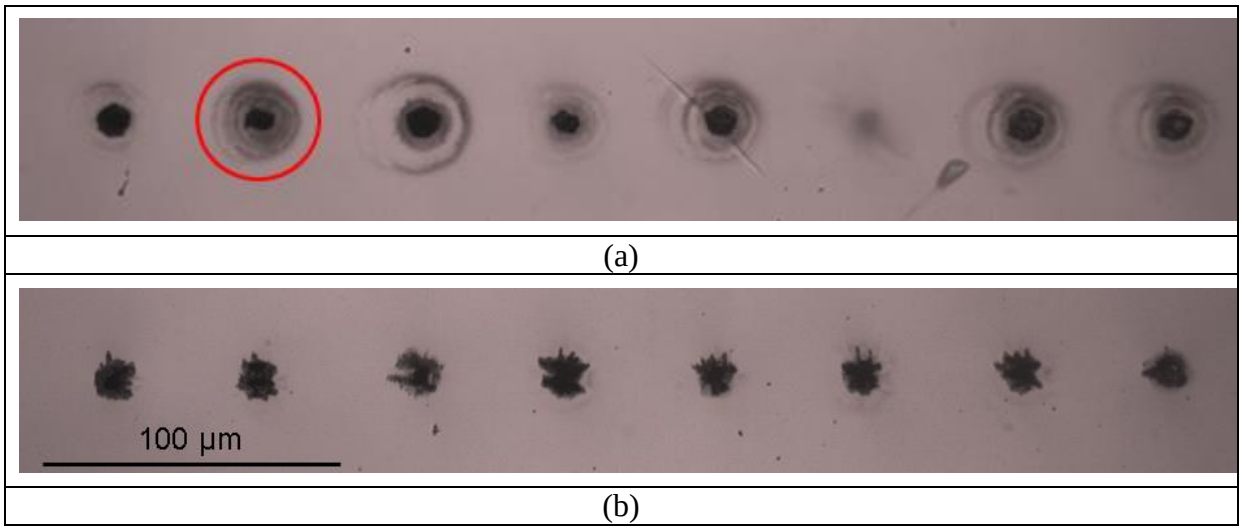

Figure 12: These sets of laser-treated channels on the a) front and b) back surface of sample 1 are all formed with a pulse energy of 4 µJ at a frequency of 250 kHz. From left to right, the number of pulses per step N is 5000, 1000, 1000, 200, 200, 100, 100, and 100. Likewise, starting from the left, the step size Δz is 6, 10, 10, 10, 10, 12, 8, and 5 µm. The red circle indicates the graphitized channel for which the Raman spectrum is provided in the second (red) curve in Figure 13

For the Raman spectrum of the channel in Figure 12, there is a distinct, strong peak around 2350 cm^{-1}, followed by an even more intense and broader feature at 3080 cm^{-1}. The difference between the two Raman spectra is due to the larger number of pulses and higher pulsation frequency used for the column in Figure 12, and the intense Raman features are attributed to photoluminescence from defects created through the laser machining process [46]. Visually, laser-treated channel from Figure 12 was roughly circular on the front face with noticeable cratering and peripheral rings, while the back was dark black and similar in shape to an amoeba or 7-point star. However, neither the 1355 cm^{-1} disordered graphite nor the 1580 cm^{-1} single-phonon, crystalline graphite Raman peaks were seen in any of the Raman spectra from sample 1.

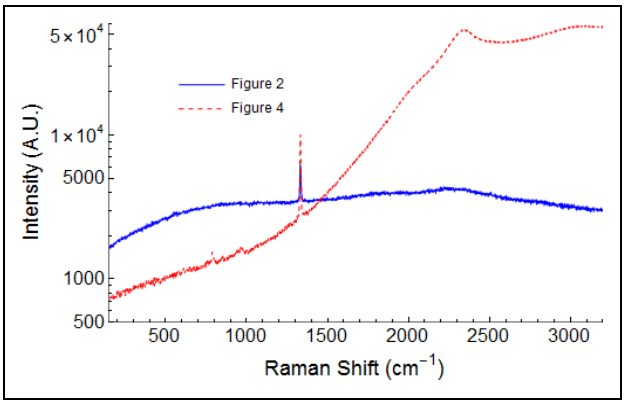

Figure 13: Raman spectra of two treated regions of sample 1. The laser pulse energy, frequency, Δz, and number of pulses per step N for each spectrum is (0.4 µJ, 33 Hz, 3 µm, and 10, solid blue curve), and (4 µJ, 250 kHz, 10 µm, and 1000, dashed red curve).

In both arrays of sample 2 (scCVD), the Raman spectra of the graphitized channels exhibited a direct correlation between the number of pulses N and the ratio I(1580)/I(1332) of intensities of graphite-like to diamond Raman peaks. Raman spectra of the laser-treated channel in column 1 of both arrays 1 and 2 and for rows 1 through 4 are provided in Figure 14. The Raman spectra were quite consistent across the four laser-treated channels of each row in the array, exhibiting both the diamond zero-phonon line around 1332 cm^{-1} and a broad distribution extending from the zero-phonon line to ~1600 cm^{-1}. The crystalline 1580 cm^{-1} peak was apparent in the spectra, which suggests that the channels partially consist of crystalline graphite, but also contain sp^2 bonded defects. The intensities of the graphite-like feature in the Raman spectra generally increased as a function of laser pulse energy, and the ratio of graphite-like to diamond peak was nearly double that of array 1. Furthermore, in array 2, a large luminescence continuum was observed, starting from ~1700 cm^{-1}. The average ratio of graphite-like to diamond Raman peak intensity for sample 2 is provided in Figure 15, where a noticeable correlation of the graphite-like to diamond peak ratio with laser energy was observed. Each data point is the average of the ratios

for the four laser-treated channels in each row of the array and the error bars show the standard deviation.

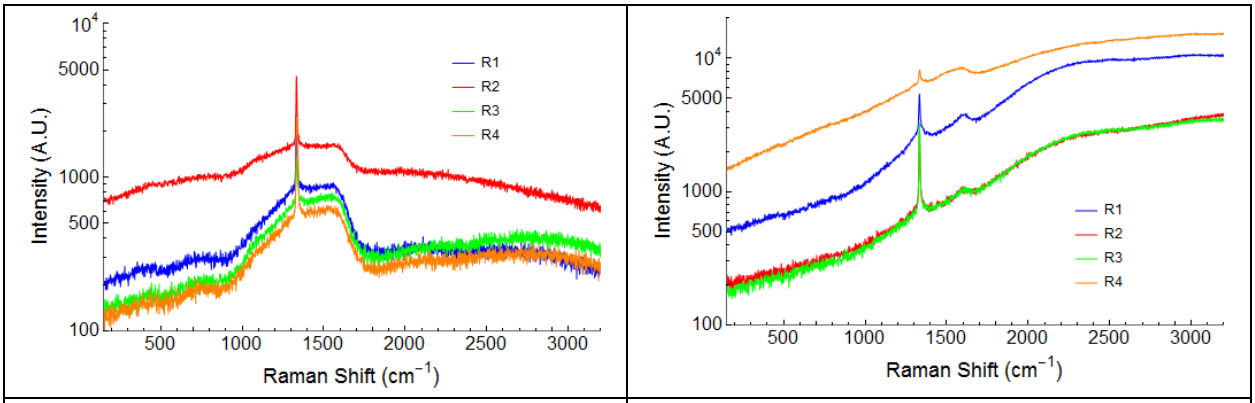

Figure 14: Raman spectra of sample 2 for channels in column 1, rows 1–4, for (a) array 1 and (b) array 2

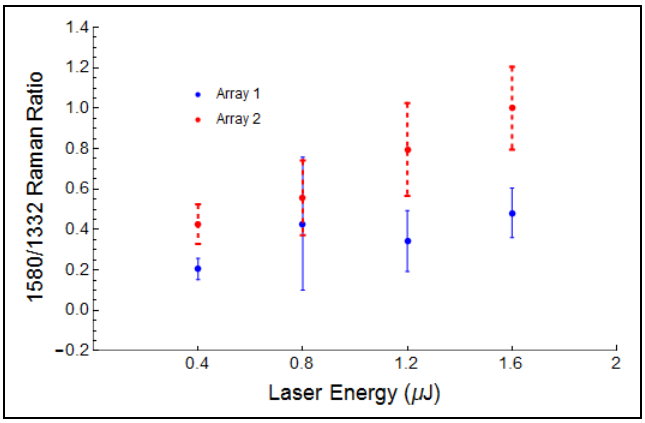

Figure 15: Average ratio of graphite-like to diamond peak intensities for each row of each array of sample 2 as a function of laser energy

The DRIE etching of sample 1 has demonstrated that the etch rate compared to the bulk diamond substrate is faster via contact profilometry, but white light interferometry was unsuccessful due to the non-reflecting nature of the laser-treated columns and the sample was inadvertently destroyed before additional investigations could take place. Results from DRIE of sample 2 consistently showed that the laser-treated channels etch considerably faster than the

surrounding diamond. The averaged etch rates from the collected data for each row in each array of sample two is provided in Figure 16. As shown, the average relative etch rate increases as a function of laser energy. The highest relative etch rates were 1.61 ± 0.02 µm/min for array 1, and 1.16 ± 0.16 µm/min for array 2. However, unexpectedly, the channels of array 1 etch faster than those of array 2, even though array 1 uses 10 laser pulses per z-step, while array 2 uses 1000 pulses per step. The apparent differences in Raman spectra collected clearly showed that the two arrays exhibit different material properties, and the lower number of pulses may have resulted to a reduced amount of reformation of sp^3 bonds, thereby increasing the relative etch rate of array 1 over array 2.

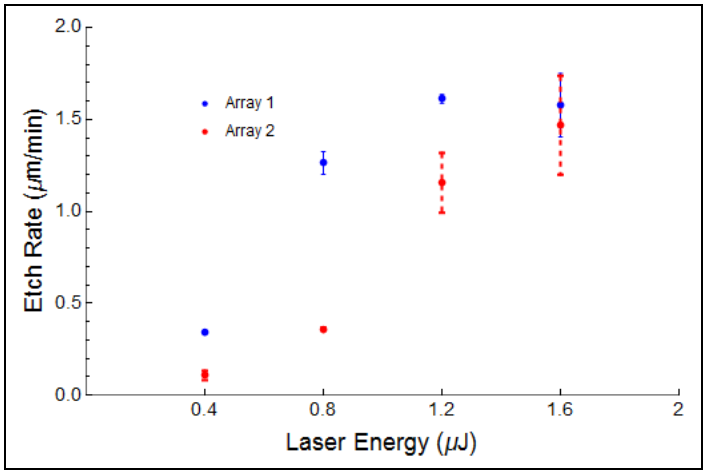

Figure 16: Average etch rate for DRIE for both arrays of sample 2 (scCVD) as a function of laser pulse energy. The error bars are the standard deviations and do not account for systematic errors from the profilometry hole-depth estimates.

2.4 Conclusions

Two chemical vapor deposition-grown diamond plates, one single-crystal and the other polycrystalline, were processed using the bulk microstructural modification technique of femtosecond-pulsed laser machining. Microscope images and confocal Raman spectra of the

processed regions revealed varying degrees of phase transformation from sp^3 bonded carbon to sp^2 bonded and disordered sp^2 bonded carbon, as ascertained by the appearance of dark graphite-looking carbon in the images and the presence in the spectra of the characteristic 1332 cm^{-1} diamond peak and a broad distribution of features from the zero-phonon line to ~1600 cm^{-1}. Many laser parameters investigated with the pcCVD diamond did not result in graphite-like peaks in the spectra but did yield an increased luminescence continuum starting from ~1700 cm^{-1}, although graphite-like discoloration was observed in the microscope images.

For sample 2, a general trend between the laser treatment energy, as well as a larger number of laser pulses per Δz, and the graphite-like to diamond peak intensity ratio was observed. However, the polycrystalline nature of sample 1 suggests that a higher rate of conversion from sp^3 to sp^2 bonded carbon should occur for the same processing parameters as sample 2, but this result was not observed.

During deep reactive ion etching (DRIE), the opposite trend from the Raman analysis was observed for sample 2, where a higher number of pulses per Δz results in a lower etch rate in scCVD diamond. The Raman spectra of array 1 showed the expected material conversion, while array 2 demonstrated a strong level of luminescence. The source of the luminescence was seemingly also the source of the reduced etch rate. Regardless of the Raman spectra, it was observed that the relative etch rate of the laser-treated columns in both polycrystalline and single-crystal diamond was significantly faster than the etch rate of the bulk diamond material, where diamond etches at a rate of no more than a few hundred nanometers per minute [47-50]. Therefore, with a suitable hard mask to protect the diamond substrate, etch rates of laser-treated columns may be as high as 2 μm/min, sufficient to create TDVs in a reasonable timeframe for a variety of applications.

Chapter 3: Realization of Through-Diamond Via Metal Electrodes for 3D Diamond Radiation Detectors

Summary

In order to create TDVs in CVD diamond plates, deep reactive ion etching (DRIE) techniques similar to those employed in the silicon industry for creating through-silicon vias (TSVs) were utilized. Two different diamonds, one optical-grade and one detector-grade, were used to establish a repeatable process for etching holes completely through the diamonds. A stainless steel (SS) foil was found to be an effective and robust etching mask for the creation of TDVs of a maximum aspect ratio of 5.0. Electroplating was used to fill the vias with a highly conductive chromium metal. The TDVs were connected with interdigitated strips on the surface of the diamond, establishing for the first time a 3D diamond radiation detector with fully metal electrodes.

3.1.1 DRIE of Silicon

DRIE of silicon for TSV fabrication utilizes a plasma etching process in which fluorine radicals chemically interact with the surface of the silicon forming a volatile reactant gas of silicon tetrafluoride. This reaction is shown below.

$$Si + 4F^* \rightarrow SiF_4 \quad (6)$$

*F** indicates the fluorine radical. In the silicon dry etching process, fluorine ions are created by introducing a fluorinated reactant gas (e.g. sulfur hexafluoride, carbon tetrafluoride, xenon difluoride, etc.) into an evacuated reaction chamber where a high frequency AC current is

directed through water-cooled induction coils wrapped around the gas inlet portion of the vacuum chamber. The resulting oscillating magnetic field dissociates SF_6 molecules into a multitude of SF_{6-x} species, sulfur compounds, and fluorine atoms and radicals [51]. A separate AC bias potential is applied to the electrode on which the silicon wafer rests, providing an electric field that directs positive ions into the surface of the silicon. A schematic of the inductively-coupled plasma reactive ion etching tool is shown in Figure 17.

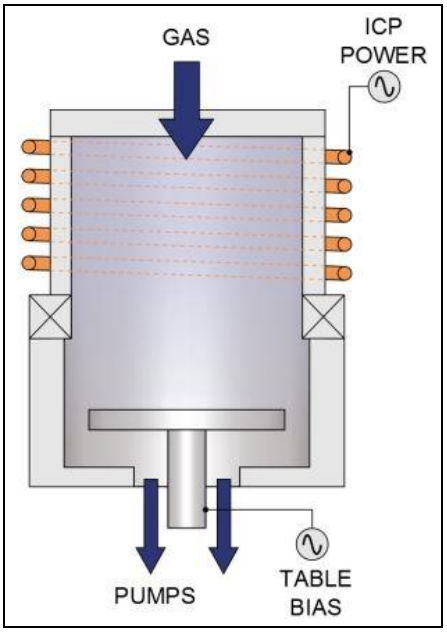

Figure 17: Schematic of the Oxford Plasmalab 100 ICP/RIE etch chamber [52]

Once the fluorine ions are created, several sequential steps must occur in order for the chemical reaction with silicon to take place:

1. The SF_6 reactant gas adsorb onto the silicon surface.
2. The gas is dissociated into fluorine atoms, which are radicalized by the energy of incoming ions and secondary electron creation.
3. Fluorine radicals react with silicon to form SiF_4.
4. SiF_4 desorbs off the silicon surface and is pumped out of the system.

Furthermore, during a DRIE process, several different etching mechanisms can take place. These are shown in Figure 18.

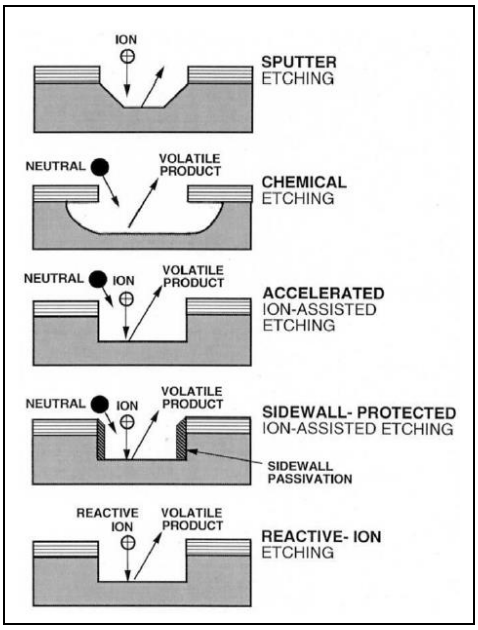

Figure 18: Different etch mechanisms of dry etching [53]

Sputter etching is the result of elastic collisions between incident ions and the substrate surface. If the energy of an incoming ion is greater than the binding energy of the substrate surface atoms, then the surface atoms are ejected away from the surface, resulting in an anisotropic etch profile. In a *chemical etch* process, such as that described in Equation 1, radicals react with the substrate surface at an equal rate in all directions, producing an isotropic etch profile. In *ion accelerated ion-assisted etching*, the accelerated ions sputter etch the substrate surface while also increasing the effectiveness of the chemical etch process. This is because the high energy ions enhance the radical adsorption and dissociation steps, increase the formation rate of reaction products by supplying energy to the surface, and/or increase the desorption rate of reactant molecules [54-

56]. The overall effect is an increased etch rate of the substrate surface and a more anisotropic etch profile.

DRIE in silicon is made possible through *sidewall-protected ion-assisted etching*. As previously mentioned, the chemical reaction in Equation 1 produces an isotropic etch profile. In order to etch truly deep (etch depths greater than tens of micrometers) features into silicon, a sophisticated process was created by the German company Robert Bosch GmbH [57]. In the famous *Bosch Process*, subsequent steps of isotropic etching of silicon and passivation of the etched sidewalls are repeated to create a "scalloped" etch profile that is highly anisotropic. The Bosch process typically produces sidewalls similar to those shown in Figure 19.

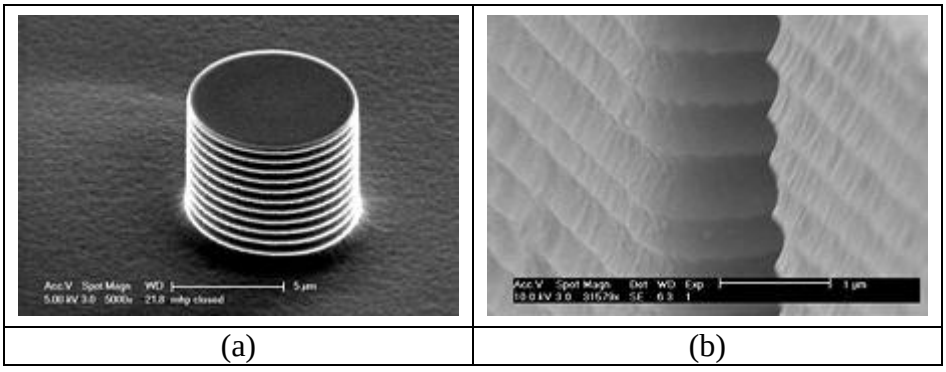

(a) (b)

Figure 19: Typical scalloped sidewall profile of the Bosch etch process [58]

3.1.2 Silicon DRIE Masks

In an ideal dry etching process, exposed regions of the substrate are etched, while regions covered by a less reactive material, often called a mask, remain unaffected. However, due to the aggressive nature of the plasma etching environment, etch masks must be very carefully selected for each etching application in order to maintain fidelity of the pattern transferred to the substrate. The selectivity of a mask is the most important parameter and is defined as the

substrate etch rate divided by the mask etch rate. Typical mask selectivities for silicon DRIE masks are around 75-100:1 for photoresists, 150-200:1 for silicon dioxide, and >5000:1 for aluminum oxide films [59].

3.2 Literature Review of Diamond Dry Etching

Reactive ion etching (RIE) of diamond has been researched for a number of different applications, including creation of AFM tips [60], fabrication of microelectromechanical structures (MEMS) [61], and diamond radiation detector fabrication [62]. Typical RIE of diamond utilizes oxygen as the *chemical etch* gas, and heavier gases are added to induce *accelerated ion-assisted etching* to increase the etch rate. The diamond dry etching reaction involves the adsorption of oxygen radicals onto the diamond surface where carbon monoxide or dioxide is formed [63]. This reaction is shown below.

$$C + O^* \rightarrow CO \tag{7}$$

During diamond RIE, numerous types of masking materials have been utilized, including sputtered or evaporated metal films [64-66], sputtered or CVD-grown ceramic films such as silicon dioxide and aluminum oxide [67, 68], photoresist [69], and spin-on glass [49]. Micromasking, in which the mask is resputtered onto the surface while etching, has been demonstrated to be an issue during diamond etching due to the low pressure and high ion energy etch environment. While a significant amount of research has been undertaken on the dry etching of diamond, the creation of TDVs in diamonds thicker than 50 μm has yet to be achieved.

The first RIE of diamond was reported by Sandhu *et al.* in 1989 when they used argon, hydrogen, and oxygen to etch thin carbon films and natural type IIa diamonds. Etch rates of 56 nm/min and 35 nm/min were achieved for the carbon films and diamonds, respectively [70].

Later, Ando *et al.* fabricated arrays of high aspect ratio (height to diameter of 8) cylindrical microstructures with an average height of 22.5 µm into HPHT, type Ib diamonds covered with a patterned aluminum mask. The diamond surface features were etched with an average material removal rate of 158 nm/min using a mixture of CF_4 and O_2 gases while also achieving a selectivity of 20 to the Al mask [66]. This work demonstrated that highly anisotropic microstructures can be etched into the surface of diamond with high fidelity. Hwang *et al.* also utilized an aluminum mask to protect HPHT diamonds during the etching of various microstructures. Argon and oxygen gases at a 1:3 ratio were used to obtain an etch rate of 666 nm/min with a selectivity of 50 to the aluminum mask [65]. While a very high Al mask etch selectivity was demonstrated, total etch time was only five minutes. The aluminum mask would have likely eroded during longer etch times due to the sputtering of oxidized aluminum.

More recently in 2013, optical gratings 4.7 µm deep were etched into both polycrystalline and single crystal diamond at a surface etch rate of 170 nm/min by Forsberg *et al*. However, the etch rate decreased to 75 nm/min at the bottom of the trench, demonstrating that the effect of ARDE is present in diamond etching. An aluminum mask was used, although it eroded before the target depth of 13.7 µm [48]. This work provides insight into exactly how difficult RIE of diamond can be due to the lack of a highly durable etch mask that is easily micropatterned. In 2016, the first mask with high selectivity in deep RIE of diamond was reported by Yunata and Aizawa during the microgrooving of CVD diamond coatings on WC(Co) substrates. The average etching rate obtained was 167 nm/min, and a depth of 19 µm was achieved using a 50 µm thick SS foil mask [71]. While the authors did not mention the selectivity of the foil mask, it is encouraging that the SS survived for 113 minutes of high density plasma etching.

3.3 Literature Review of 3D Diamond Detectors

The first three-dimensional diamond detector to be fabricated was reported on by Oh *et al* in 2013 [43]. Graphitic wire electrodes were created through the bulk of a 500 μm thick diamond using a nitrogen laser with 3 nanosecond pulse durations. The electrodes were connected by evaporated aluminum strips on the diamond surface. A picture of the detector is shown in Figure 20.

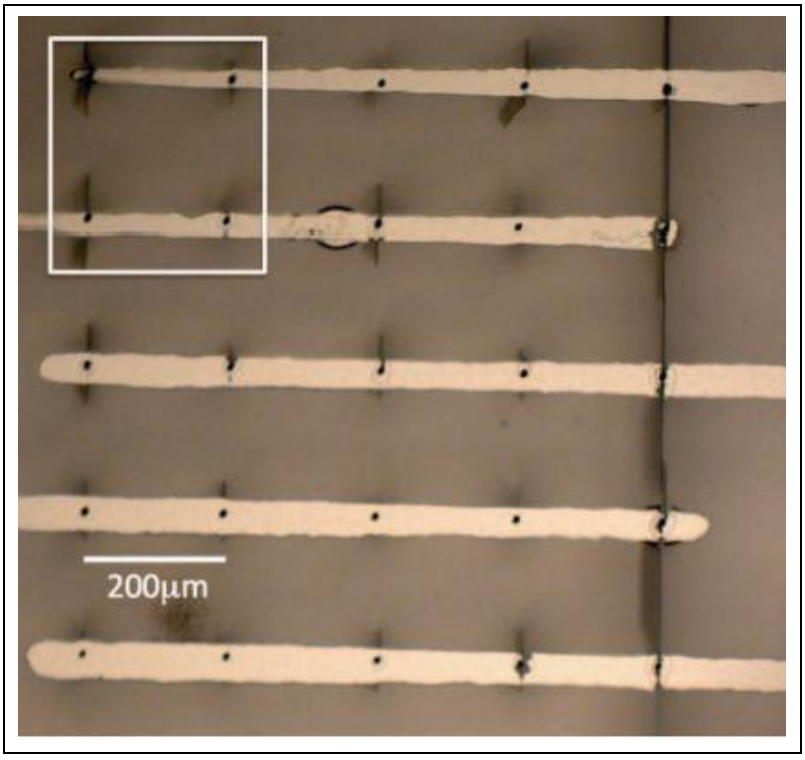

Figure 20: 3D diamond detector with graphitic wire electrodes [43]

Electric current generated by 15 keV X-Rays was measured between the interdigitated Al strips in the region ascribed by the white box in Figure 20. More rigorous testing of 3D diamond detectors fabricated through laser machining was conducted by Bachmair *et al.* who tested a device in a 120 GeV proton beam [72]. A direct comparison of the 3D diamond's performance to

a planar diamond detector was accomplished by creating both planar and 3D graphitic electrodes on the same sample. The 3D device architecture collected a similar amount of charge to the planar electrode geometry, as shown in Figure 21.

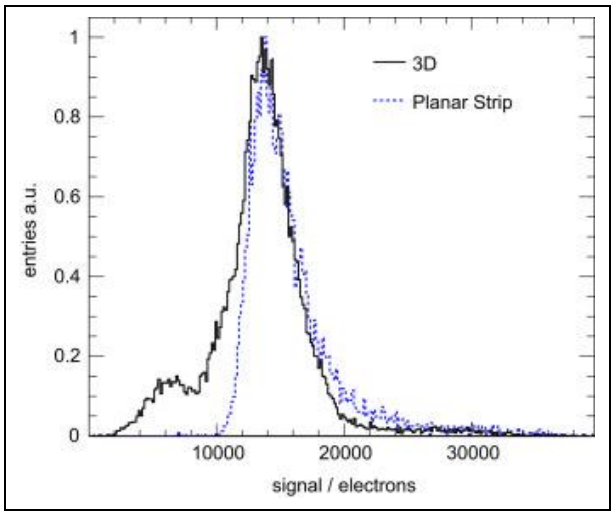

Figure 21: Response of 3D and planar geometry to 120 GeV proton irradiation [72]

Finally, the radiation hardness of the 3D electrode geometry in polycrystalline diamond detectors has recently been studied by Lagomarsino *et al*. It was demonstrated that after neutron irradiation 3D diamond detectors collected an average of three times more charge relative to the planar diamond detectors [73]. The degradation of CCE in both diamond electrode geometries as a function of 1 MeV neutron equivalent fluence is shown in Figure 22.

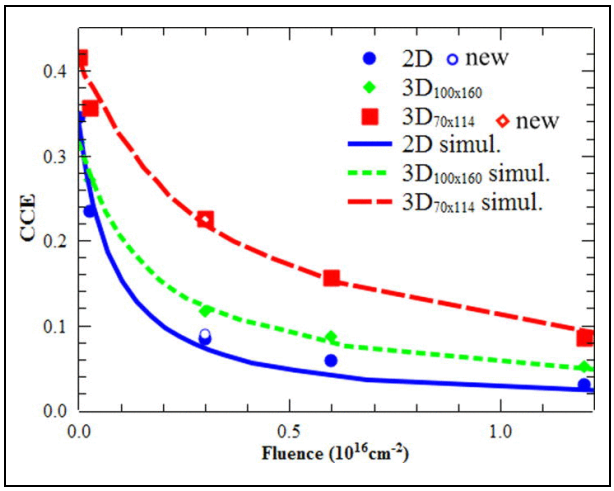

Figure 22: CCE as a function of 1 MeV equivalent neutron fluence [73]

Clearly the 3D electrode geometry increased the amount of charge that was collected even at high neutron fluences.

3.4 Creation of a 3D Diamond Radiation Detector with Metal Electrodes

While the graphitic wires created by femtosecond-pulsed laser machining for current 3D diamond are a proven working technology, there exists room for improvement concerning device throughput and the conductivity of the readout electrodes. The throughput of the graphitic wire manufacturing process is inherently low, since each graphite channel must be laser treated individually to convert the carbon sp^3 bonds to sp^2 bonds. Raman spectroscopy of the processed regions has shown that the phase transformation is not 100% efficient [41]. The resulting graphite has a resistivity that is still roughly three orders of magnitude higher than crystalline graphite [41, 43]. In 3D diamond detectors, increased resistance between the detector and the preamplification stage results in Johnson noise, decreasing the signal-to-noise (S/N) ratio of the detector. Furthermore, the greater resistance of the graphite wires reduces the speed at which charge can be readout from the detectors. A 3D diamond detector with TDVs composed of metal

electrodes could exhibit drastically reduced charge readout time and enhanced S/N performance compared to 3D diamond detectors containing graphitic electrodes.

In order to create high aspect ratio TDVs in diamond plates that are sufficiently thick for high energy particle detection, DRIE similar to that performed in the TSV industry was performed on two single crystal diamond plates. The properties of the diamonds used to test the feasibility of creating TDVs in thick diamond plates are shown in Table 4.

Table 4: Properties of Diamonds used for TDV creation

Sample Name	Dimensions (mm^3)	Classification	Manufacturer
Beta	3.0x3.0x0.3	Type Ib; Optical Grade	Scio Diamond
Alpha	2.0x2.0x0.3	Type IIa; Electronic Grade	Element Six

First, to determine the etching parameters that yield the highest etch rate during diamond DRIE, a parametric study was conducted of the diamond material removal rate as a function of chamber pressure, RF power, and argon to oxygen inlet gas ratio. All etching is performed in an Oxford Plasmalab 100 ICP-RIE tool (discussed in Section 3.1.1) on type Ib, single crystal 3.0x3.0x1.2 mm^3 diamond substrates with half of the diamond surface masked with Kapton tape. The step height between the masked and unmasked region was determined using a KLA-Tencor P-6 stylus profilometer. The samples were profiled in three locations across the step in order to calculate the variance of the step height and associated etch rate. Chamber pressure largely dictates the regime of etching (i.e. *chemical* or *ion-assisted etching*) because lower etching pressures (<10 mTorr) result in increased average ion energies and mean free paths and a highly anisotropic etch profile. At higher pressures, the higher concentration of atoms in the system induces scattering among species in the system, resulting in reduced ion energies and mean free

paths and producing a more isotropic etch profile. For these reasons, the effect of chamber pressure on the diamond etch rate was first to be analyzed. The ICP-RIE parameters other than chamber pressure were kept constant and are listed in Table 5.

Table 5: Base DRIE Parameters for Diamond Etch Rate Parametric Study

ICP Power (Watts)	RF Power (Watts)	O_2 Flow Rate (sccm)	Table Temperature (°C)	He Backing Pressure (Torr)
2000	150	50	20	5.0

The ICP-RIE etches were performed for 5 minutes each at chamber pressures of 1, 3, 5, 10, 20, 40, 60, and 80 mTorr. The resulting diamond etch rate as a function of chamber pressure is shown in Figure 23.

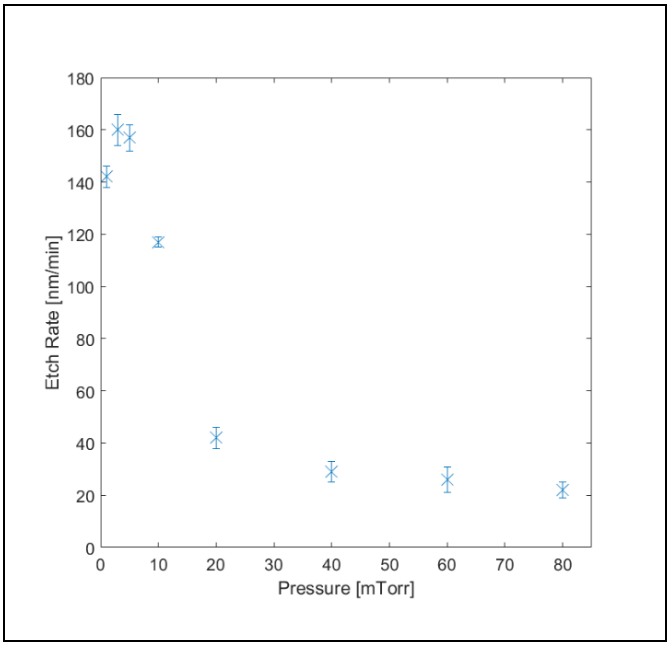

Figure 23: Diamond etch rate as a function of chamber pressure

The diamond etch rate is clearly higher at lower pressures, reaching a maximum of 160 ± 6 nm/min at 3 mTorr. Since the material removal rate of diamond is greater at lower pressures, the diamond etching process is induced by the ion-assisted chemical etching of carbon by oxygen radicals. In ion-assisted-etching, the increased surface temperature caused by kinetic energy transfer from heavy argon ions enhances reaction product desorption. Furthermore, the surface area of the region being etched is increased because heavy ion bombardment roughens the surface.

Next, the effect of RF power on the diamond etch rate was studied. Higher RF powers increase the electric potential that drives ions into the diamond surface. This potential of negative polarity is the called the DC table bias and is a result of electrons in the plasma being much more mobile than positive ions. Since diamond etching is an *accelerated ion-assisted* process, logic would follow that the etch rate should be higher with increasing impinging ion energies. This logic is valid and is proved by the results of Figure 24.

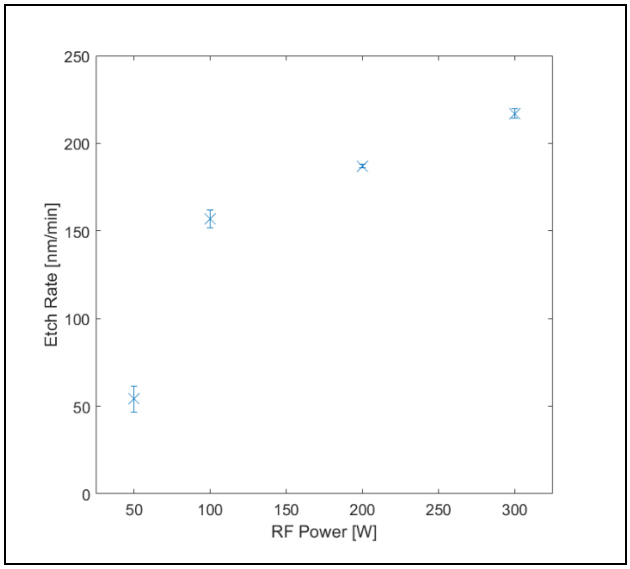

Figure 24: Diamond etch rate as a function of RF power

At 5 mTorr and an RF power of 300 Watts, a maximum etch rate of 217 ± 2.7 nm/min is achieved. Higher RF powers increase the diamond etch rate due to the higher energy of oxygen ions bombarding the diamond surface. Average ion energies were increased at large RF table power levels due to the increased DC bias. The last parametric study performed was on the effect of adding a small amount of argon gas to potentially increase the etch rate through heavier ion bombardment. The results showed an increase in diamond etch rate at argon concentrations up 15%; further increasing the argon decreased the etch rate as shown in Figure 25.

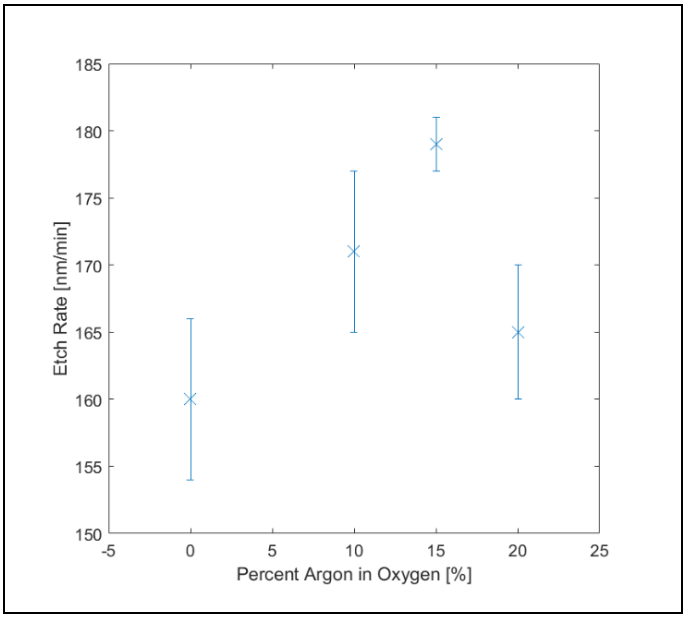

Figure 25: Diamond etch rate as a function of argon gas percentage

A maximum diamond etch rate of 179 ±2 nm/min was achieved with 15% argon, 85% oxygen, an RF power of 100 Watts, and a chamber pressure of 3 mTorr. Introducing argon, which is 2.5 times heavier than oxygen, to the gas mix further increases the average ion energy impinging upon the diamond surface. While adding a small amount of argon increases the diamond etch rate, too much argon will negatively affect the etch rate. This is because the dry etching of

diamond is driven by the reaction in Equation 1. Once the concentration of oxygen gas drops, due to replacing O_2 with Ar, the rate of the diamond *chemical etch* mechanism begins to diminish as the average oxygen radical concentration drops.

3.4.1 Diamond DRIE Etch Mask

Since the dry etching of diamond has been demonstrated to be an *accelerated ion-assisted etching* process, a robust mask that can survive tens of hours of energetic ion bombardment had to be engineered. As discussed in Section 1.3.2, an etch mask composed of a SS foil has shown the highest etch selectivity for DRIE of diamond. However, standard dry etching processes cannot etch SS foil, due to the highly-alloyed composition of the steel matrix. Wet etching of SS foils with high fidelity patterns is possible using standard photolithography and etching in ferric chloride. The resulting etch profile is isotropic, which limits the height to diameter ratio that can etched into the foil.

A unique solution to this problem was found in a technique called electrical discharge machining (EDM). During EDM of a foil or other geometry, a dielectric fluid is placed between the EDM tool wire and the foil surface. The high electric field and rapid discharge of current between the EDM wire and the surface to be machined causes the dielectric to break down, which allows the current to "spark erode" the surface. Once the pulse of current has ended, the dielectric fluid flows into the machined area carrying away ablated material. Because the size of EDM tool wire tips can vary from tens to hundreds of microns, the process is highly versatile. To test the feasibility of utilizing the EDM process to manufacture diamond DRIE etch masks, a 4x4 array of 100 μm diameter circles spaced 500 μm apart was machined into a 50 μm thick SS foil. A micrograph of the foil mask is shown in Figure 26.

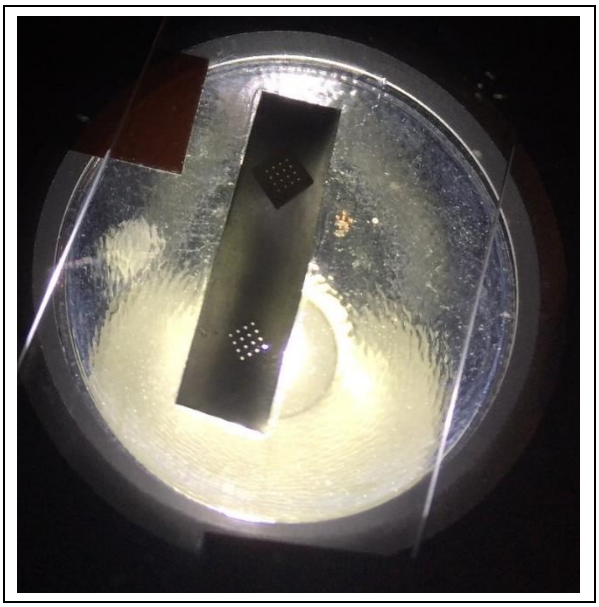

Figure 26: Optical micrograph of SS mask used for DRIE of sample *Beta*

The dimensions of the foil were designed to fully cover diamond sample *Beta* and were approximately 5 mm wide by 8 mm long. Alignment of the foil and sample *Beta* was accomplished using a microscope with backside illumination, and photoresist was used secured *Beta* to the foil, and the photoresist was hardened for 1 minute at 100°C while applying pressure to the foil-diamond stack to minimize the gap between the two. Photoresist was chosen as the preferred adhesive because it is easy to apply and is readily removed in oxygen plasma.

3.4.2 Etching High Aspect Ratio Diamond Microchannels

In the Oxford Plasmalab 100 system at the Center for Nanophase Materials Sciences (CNMS) at the Oak Ridge National Laboratory, only 4-inch diameter substrates (generally silicon wafers) can be loaded into the chamber. Thus, sample *Beta* was attached to a 4-inch silicon wafer using thermally conductive Krytox vacuum grease. Multiple etch sessions were utilized to etch sample *Beta* followed by depth profiling to establish a representative etch rate. The ICP-RIE parameters used to etch *Beta* during the first etch session are shown in Table 6.

Table 6: DRIE parameters used to etch sample *Beta* after attaching the mask for the first time

ICP Power (Watts)	RF Power (Watts)	Chamber Pressure (mTorr)	O_2 Flow Rate (sccm)	Table Temperature (°C)	He Backing Pressure (Torr)
3000	100	10	80	20	5.0

After etching sample *Beta* for 135 minutes, the SS foil mask fell off while examining the depth of the holes and the condition of the mask. Due to the extreme depth of the etch pit and the increased surface roughness of the surface at the bottom of the pit, very little light was reflected out the holes during optical microscopy, making it impossible to estimate the hole depth using this method. The SS foil mask was measured using a micrometer to be around 49 µm. Since the foil thickness had not decreased more than 1 µm, it was determined to be a suitable mask for DRIE of diamond.

To resume etching of the diamond the SS foil was reattached to sample *Beta* using photoresist. However, alignment of the 4x4 array of holes in the foil to the holes already etched into the diamond surface proved to be quite difficult. Thus, a new set of holes was etched using slightly different DRIE parameters, as shown in Table 7.

Table 7: DRIE parameters used to etch sample *Beta* after attaching the mask for the second time

ICP Power (Watts)	RF Power (Watts)	Chamber Pressure (mTorr)	O_2 Flow Rate (sccm)	Ar Flow Rate (sccm)	Table Temperature (°C)	He Backing Pressure (Torr)
2800	150	10	100	10	20	5.0

Argon was added to gas mix, as well as increasing the RF power, in an attempt to increase the etch rate. The total ICP power level was decreased at request of the Staff scientists at CNMS, since the ICP generator should not be continuously operated at its maximum output at 3 kW.

Sample *Beta* was etched for 1,265 minutes, or about 21 hours, before the SS foil was removed to determine the depth of the holes. Before examining the diamond under the optical microscope, a 100 nm layer of chromium metal was sputtered onto the surface and into the holes of sample *Beta*. This was done to provide a more reflective surface at the bottom of the holes for optical microscope viewing. As is shown in the optical micrograph in Figure 27, the deposited chromium metal proved very useful for imaging the bottom of the etched holes.

Utilizing the height scale on the optical microscope's stage, it was estimated that the first and second etch hole depths were about 20 µm and 100 µm, respectively. The average etch rate for each etch session was calculated to be 133 nm/min and 79.1 nm/min, respectively. Comparing to the etch rates determined in Section 3.4.1.1, the average etch rate to obtain significantly deep etch holes in diamond is much lower than the etch rate at the surface. This effect, called aspect ratio dependent etching, is commonly observed in DRIE of silicon and is primarily due to the reduced ion flux at the bottom of the etch hole. At this point, a Zeiss Merlin scanning electron microscope (SEM) was used to image the surface of sample *Beta*. The holes in *Beta* were imaged at incident electron angles of 0° and 30° to estimate the depth. SEM micrographs of the 20 µm holes in sample *Beta* are shown in Figure 28. Using the formula $d=h/\sin(90°-\theta)$, where d is the hole depth, h is the height measured at an incident electron angle of θ, the depths of the holes are estimated to be around 20 µm, verifying the depth estimated using the microscope stage height scale.

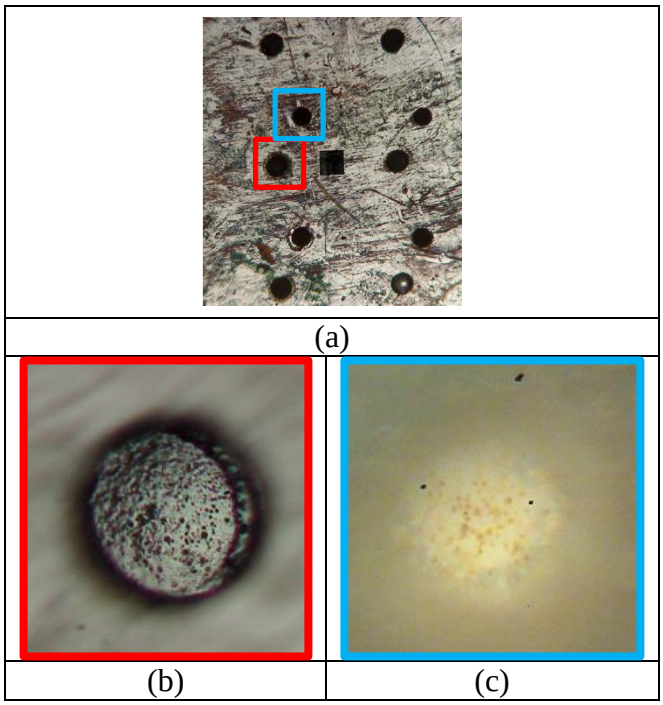

Figure 27: (a) Surface of sample *Beta* after Cr deposition, (b) bottom of 20 µm deep hole created during the first etch, and (c) bottom of 100 µm hole created during the second etch

Unfortunately, this depth estimation technique could not be utilized on the deeper holes because the bottoms of the holes were not visible when the sample stage was tilted. SEM micrographs of the entire surface of sample *Beta* and of the 100 µm deep holes are shown in Figure 29. The bottoms of the holes were imaged to determine if the etch profile was truly anisotropic as the depth increases. Since the diameter does not decrease from the top to the bottom of the hole, the etch was determined to be truly anisotropic.

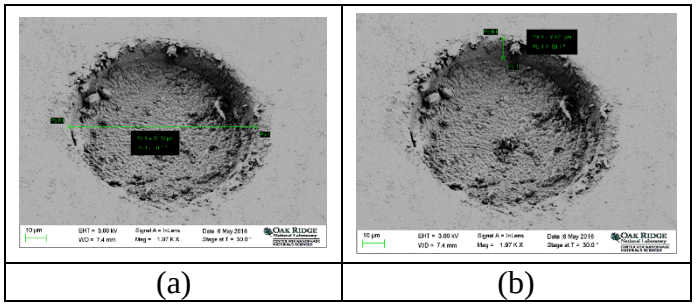

Figure 28: SEM micrograph measuring the (a) width and (b) height of one etch hole in sample *Beta*

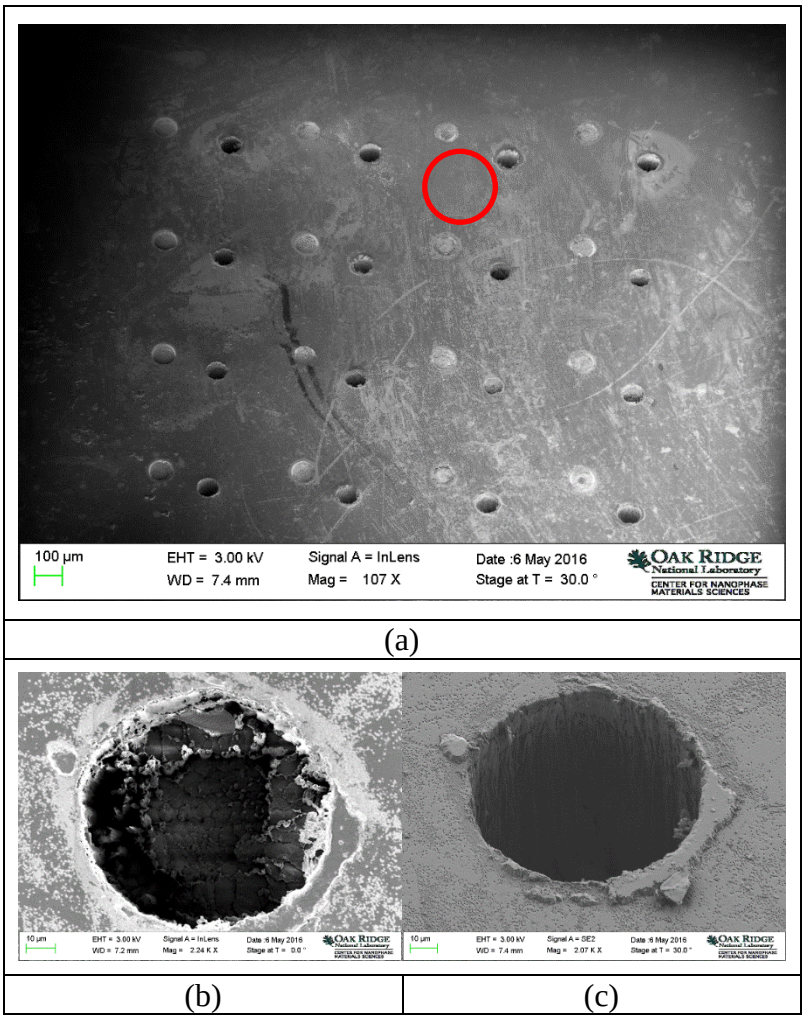

Figure 29: SEM micrograph of (a) the entire surface of sample *Beta*, (b) bottom of the indicated hole, and (c) a tilted image of the indicated hole

Sample *Beta* was flipped over at this point in order to etch the sample bulk with no mask. After 10 hours of thinning in the ICP-RIE plasma, the deeper holes had become exposed from the back side of the diamond, creating TDVs with an aspect ratio of 1.0 in a 100 µm thick diamond. The TDVs in sample *Beta* with topside (a) and backside (b) microscope illumination are shown in Figure 30.

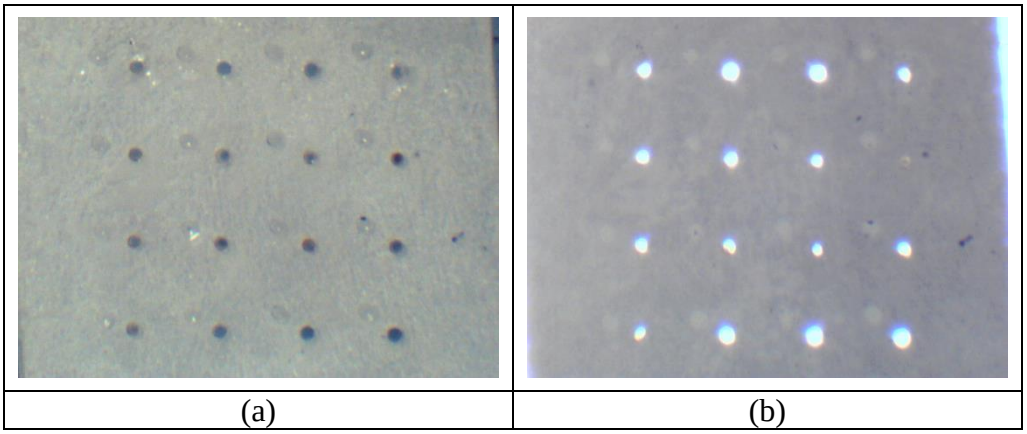

(a) (b)

Figure 30: (a) Topside microscope illumination and (b) backside microscope illumination of TDVs in sample Beta

Although thinning diamonds using strictly dry etching can be effective, one negative effect of this method is a drastic increase in surface roughness. The as-received average surface roughness, R_a, of sample *Beta* was around 30 nm. After thinning the diamond in high energy oxygen and argon plasma, the R_a value increased to around 1.5 µm. This extreme increase in surface roughness on the backside of sample *Beta* is shown in the micrographs in Figure 31.

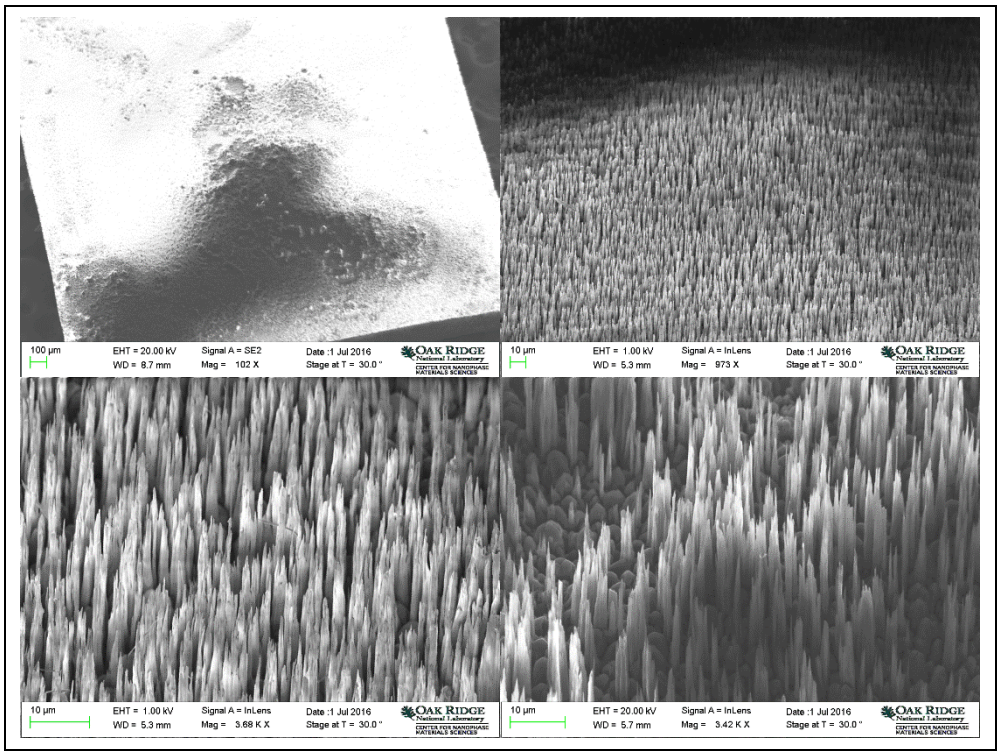

Figure 31: SEM micrograph of the entire surface of sample *Beta* at various magnifications

The needle-like structures were the result of the extreme etching environment experienced at the surface of the diamond. Using energy dispersive x-ray spectroscopy (EDS), the elemental composition of the needles was analyzed to confirm that the microstructures were indeed carbonaceous, rather than resputtered silicon dioxide or aluminum oxide. The EDS spectrum of the carbon needles is shown in Figure 32. Oxides of silicon and aluminum were present (likely from alumina-masked silicon etching routinely performed in the chamber), but it was clear that the needles were composed of carbon. It was likely that the micromasking of sputtered oxides contributed to the creation of these microstructures and the overall increase in the surface roughness of diamonds thinned using ICP-RIE.

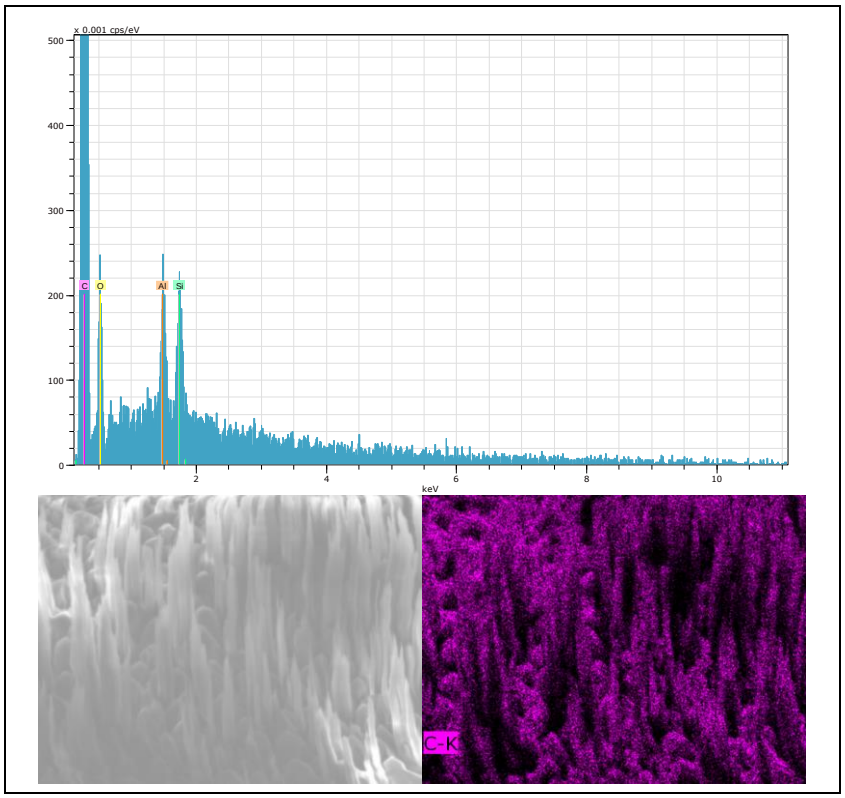

Figure 32: SEM EDS spectrum with the carbon K-edge X-ray emission sites highlighted in purple

With the success of TDV creation in a type Ib diamond, it was time to test the process on an electronic grade, type IIa diamond: sample *Alpha*. In order to fabricate a new SS mask, EDM was again used to make another 4x4 array of holes in a 50 µm thick foil. The holes were 30 µm in diameter and were equally spaced at a distance of 100 µm. An optical micrograph of the SS foil mask is shown in Figure 33. Sample *Alpha* and the new foil mask were attached to each other and to a silicon carrier wafer in the same method as described in Section 4.1.2. For the first 325 minutes (5.4 hours) of etching, the DRIE parameters listed in Table 8 were used.

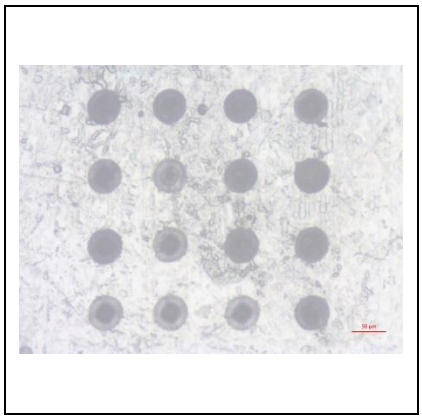

Figure 33: Optical micrograph of SS mask used for DRIE of sample Alpha

Sample *Alpha* and the new foil mask were attached to each other and to a silicon carrier wafer in the same method as described in Section 4.1.2. For the first 325 minutes (5.4 hours) of etching, the DRIE parameters listed in Table 8 were used.

Table 8: DRIE parameters used to etch sample *Beta* after attaching the mask for the second time

ICP Power (Watts)	RF Power (Watts)	Chamber Pressure (mTorr)	O_2 Flow Rate (sccm)	Table Temperature (°C)	He Backing Pressure (Torr)
2800	100	1	20	20	5.0

After 5.4 hours of etching, the ICP power level was reduced to 2 kW at the request of CNMS staff scientists. Due to the unusually long processing times required, the diamond etching was beginning to take a toll on the Oxford Plasmalab 100 ICP-RIE tool. After 12.5 total hours of etching sample *Alpha*, the pressure was increased to 5 mTorr due to a plasma instability at 1 mTorr. After 19.8 total hours of etching, argon at 5 sccm was added to the gas mix, and the pressure was decreased to 3 mTorr. This was done to increase the anisotropic nature of the etch profile, which was determined under an optical microscope to be somewhat tapered. Finally, after 24.7 total hours of sample etching, the sample was removed from the silicon wafer and the

foil mask was taken off the diamond. *Alpha* was then imaged in the same Zeiss Merlin SEM as *Beta*. The micrographs of sample *Alpha* are shown in Figure 34.

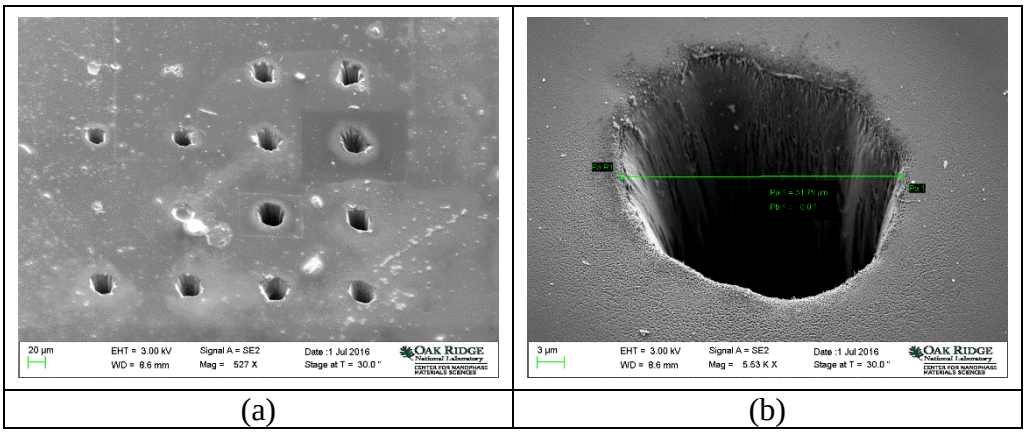

(a) (b)

Figure 34: SEM micrographs of (a) the etched holes and (b) the measurement of one hole width in sample *Alpha*

It can be seen in Figure 34 that only 13 of the 16 holes have etched into the surface of *Alpha*, likely due to a very thin layer of the SS mask remaining that was not seen before the mask was attached. The holes have an average diameter of 31 micrometers. At this point, sample *Alpha* was flipped over and thinned using ICP-RIE, which took an additional 20 hours. As with sample *Beta*, significant roughening of the back side of the diamond was observed after plasma thinning. At this point the holes penetrated the entire 150 µm thick electronic-grade diamond. An average etch rate of 101 nm/min was achieved during TDV etching with a final aspect ratio of 5.0. An optical micrograph of the 31 µm diameter TDVs through the 150 µm remaining thickness of sample *Alpha* is shown in Figure 35. A micrograph of sample *Alpha* with backside illumination is shown in Figure 36. The increase in surface roughness on the back side of the diamond is apparent as the diamond is no longer transparent.

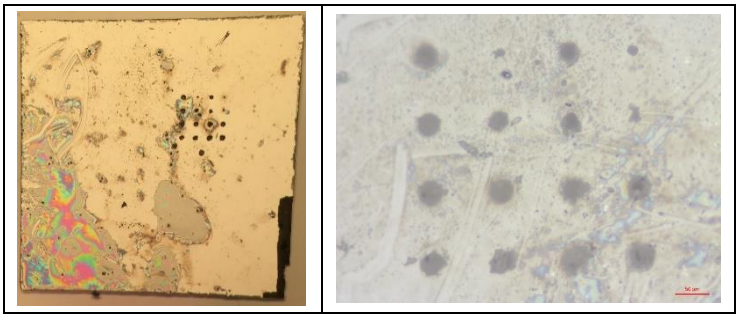

(a) (b)

Figure 35: Optical micrograph of (a) the entire sample surface and (b) the region with etched TDVs

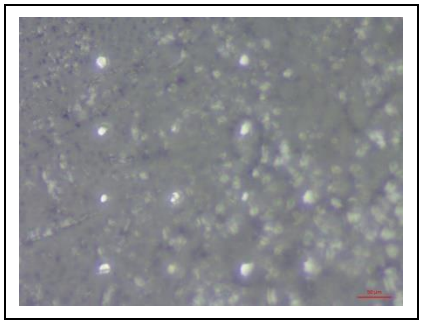

Figure 36: Optical micrograph of TDVs in sample *Alpha* with backside illumination

3.4.3 Electroplating of TDVs

In order to create metal electrodes in the TDVs, electroplating was chosen as a suitable deposition process, since high aspect ratio TSVs are regularly filled using copper electroplating [44, 45]. Chromium metal has been shown to form reliable Ohmic contacts to diamond [74, 75]. Furthermore, chromium has been deposited using electroplating since 1924 [76]. Thus, it was decided that a hexavalent chromium electrodeposition process was the most likely to succeed in filling high aspect ratio TDVs with metal. Chromium electroplating relies on the reduction of Cr^{6+} ions in a chromic acid and sulfuric acid solution through a DC current applied to the anode, which is also in the solution. Chromium metal is then deposited on the cathode in the solution.

Before chromium electroplating the diamond samples, circular TSVs, 50 μm in diameter, were etched into 5.0x5.0x0.3 mm^3 silicon chips in order to test the electrodeposition process. The silicon chips were patterned with an 80 nanometer thick chromium metal etch mask prior to DRIE. Prior to electroplating, organic contaminants were removed by boiling the silicon chip for 15 minutes in a 5:1:1 solution of deionized water, 30% NH_4OH, and 30% H_2O_2 at 70°. Bottom-up electroplating was utilized to fill the TSVs with chromium metal. In bottom-up electrodeposition, the silicon wafer with through-vias is attached to a metallized silicon wafer and placed in the electroplating solution. Ions in the solution are driven deep into the TSVs by the applied electric field, where they reduce to metal at the surface of the conductive carrier wafer. This process repeats itself until the metal deposit is thick enough to fill the empty via. In order to provide the small silicon chips with a conductive carrier wafer, the chips were attached to copper printed circuit boards (PCBs) using Kapton tape. The copper PCB is then soldered to a solid core insulated wire which is attached to a Keithley 2400 SourceMeter DC power supply. A 5.0x5.0x0.3 mm^3 silicon chip with 25 μm diameter through-holes is shown on a backside illuminated microscope in Figure 37.

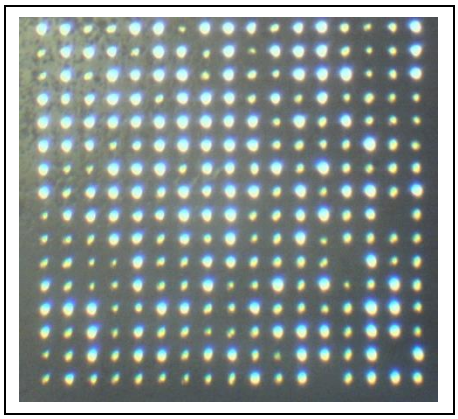

Figure 37: Backside illuminated 25 μm diameter TSVs in a 5.0x5.0x0.3 mm Si chip

A silicon chip before and after electroplating is shown in Figure 38.

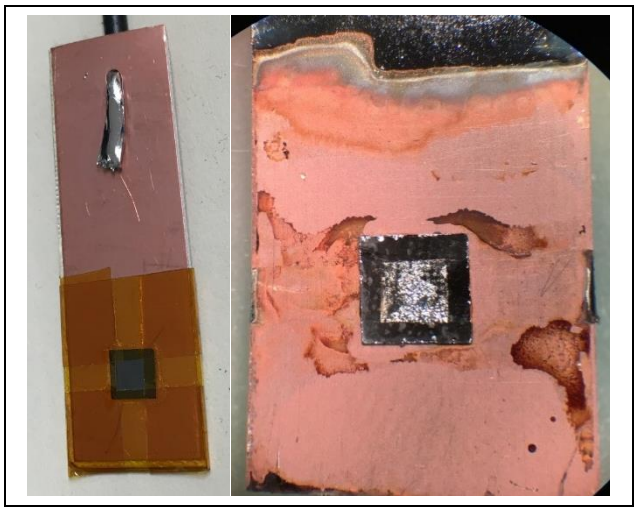

Figure 38: Silicon chip with TSVs before and after Cr electroplating

As can be seen, the Kapton tape acts as an effective electrodeposition mask. An optical micrograph of the electroplated TSV and the copper PCB carrier wafer is shown in Figure 39.

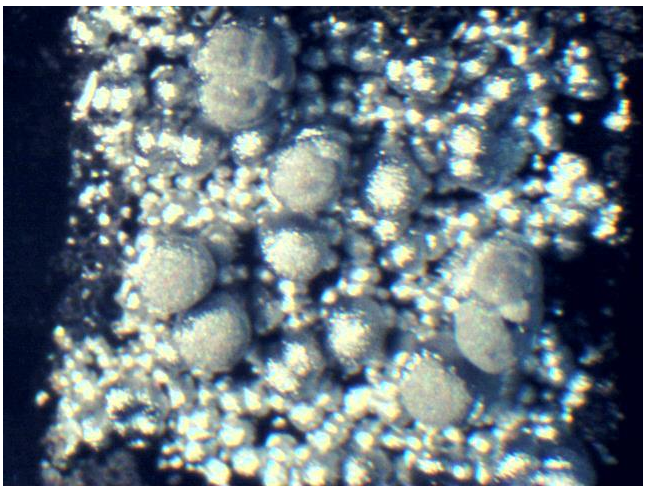

(a)

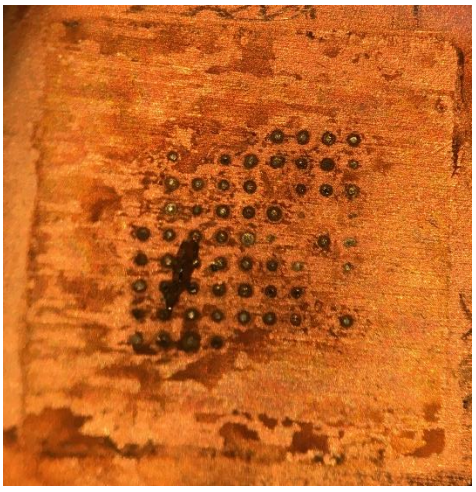

(b)

Figure 39: Optical micrographs of the (a) electroplated TSVs and (b) electroplated PCB carrier wafer

Chromium electroplating was conducted at 0.2 A/cm^2 and 55°C. The chromium metal clearly penetrates the full thickness of the Si chip. On the PCB carrier wafer, chromium metal nucleation points are visible where TSVs were present.

Prior to electroplating sample *Beta*, organic contaminants were removed by boiling sample *Beta* at 70°C for 15 minutes in a 5:1:1 solution of deionized water, 30% NH_4OH, and 30% H_2O_2. The diamond was then secured to the copper PCB using Kapton tape. Chromium electroplating was conducted at 0.2 A/cm^2 and 55°C. An optical micrograph showing electroplated TDVs in *Beta* is shown in Figure 40.

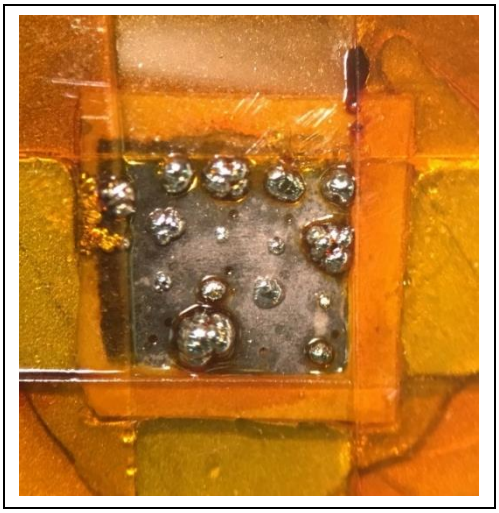

Figure 40: Sample Beta with Cr electroplated TDVs

The TDVs penetrated the full thickness of sample *Beta* and excess chromium metal deposited around the vias. Using 0.1 µm Ra diamond lapping pads, protruding chromium metal was polished back and planarized with the diamond surface. An optical micrograph of the polished, electroplated surface of sample *Beta* is shown in Figure 41.

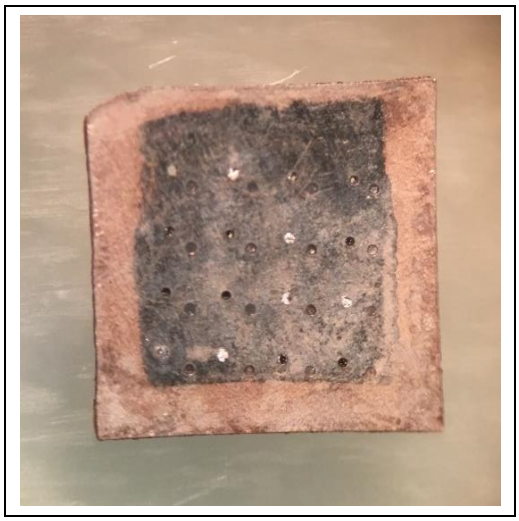

Figure 41: Sample *Beta* after polishing and planarizing the electroplated TDVs

After the success of filling the 25 µm diameter TSVs and 100 µm diameter TDVs, electroplating of sample *Alpha* was attempted. Prior to electroplating, the diamond was cleaned in the same aforementioned acid bath and was mounted onto a PCB board. The same bottom-up electroplating methods and conditions as used for filling TDVs in sample *Beta* were used. However, after multiple plating attempts, chromium metal was simply not depositing in the bottom of the holes in sample *Alpha*. To alleviate this issue, a different electroplating technique used in high aspect ratio TSV filling was employed. In this method, called conformal electroplating, a thin metal layer is deposited onto the surface of the diamond and into the open vias using physical or thermal thin film deposition. This metal layer conducts the applied DC current and promotes nucleation of the electroplated metal deep within the vias. As is shown in Figure 42, conformal electroplating also has the advantage of reduced deposition time as the width of vias is almost always smaller than their height.

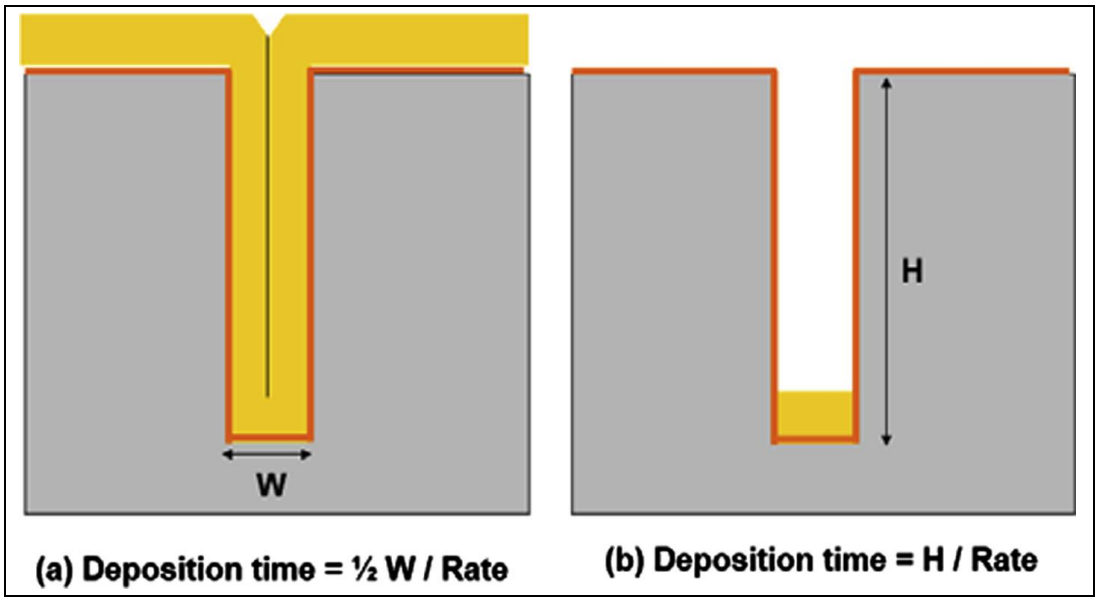

Figure 42: Depiction of (a) bottom-up and (b) conformal electroplating [75]

In order to provide a conductive metal film for conformal electroplating of sample *Alpha*, 50 nm of chromium followed by 100 nm gold was deposited onto the diamond using DC and RF sputtering, respectively. The diamond was then attached to the copper-plated PCB using a conductive aluminum tape in order to establish an electrical connection between the copper board and the sputtered Cr/Au film within the TDVs. This aluminum tape was then covered with Kapton tape. An optical micrograph of the sample *Alpha* after electroplating is shown in Figure 43.

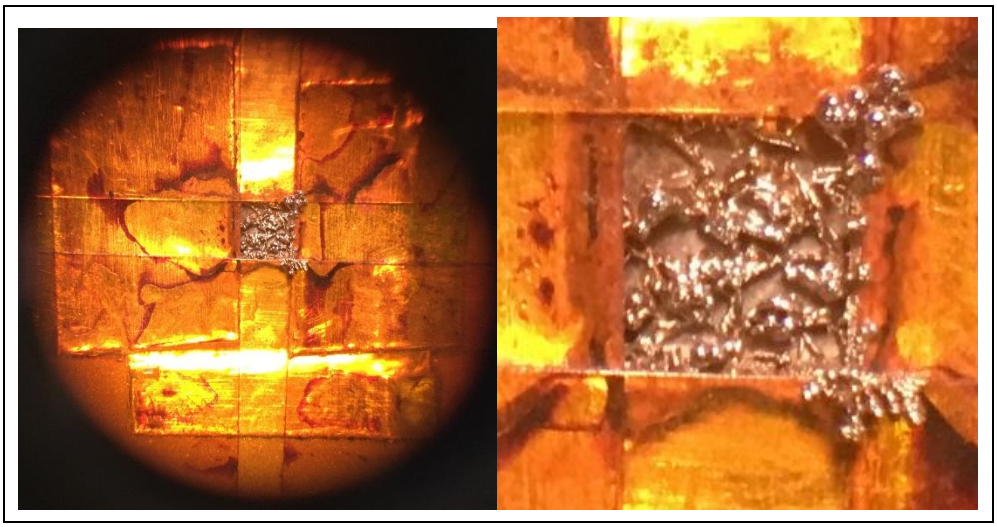

Figure 43: Optical micrograph of sample *Alpha* after conformal chromium electroplating

During electroplating, excess chromium metal grew from the TDVs, which was then polished back using a 0.1 µm Ra diamond lapping pad. The metallized and planarized TDVs of chromium metal are shown in Figure 44.

3.4.4 Detector Fabrication

Before using sample *Alpha* as an electrical device, the individual TDVs were connected using an interdigitated metal readout pattern.

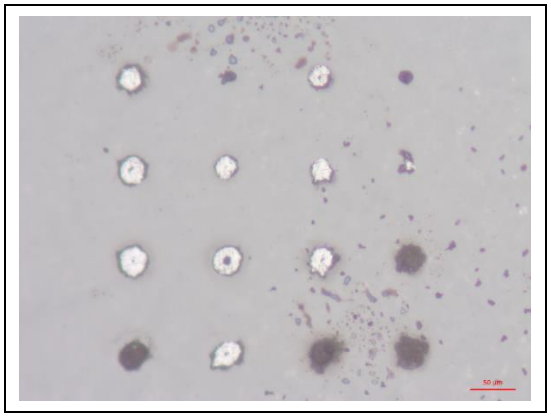

Figure 44: Sample Alpha with Cr metal TDVs

The readout pattern was designed to accommodate the successfully electroplated TDVs and was applied using conventional photolithography techniques. First, a photosensitive chemical compound, called photoresist, is dispensed onto the surface of the diamond. The photoresist is distributed in an even layer across the diamond surface by spinning the diamond at 5000 rpm. After baking the diamond on a hot plate to removal residual solvents in the photoresist, the photoresist is exposed to ultraviolet (UV) light. A photomask containing the pattern to be transferred to the diamond prevents the UV light from reaching certain regions of the photoresist. After developing the photoresist, the area to be metallized is cleared of photoresist, allowing for metal to be deposited directly onto the diamond surface. Only the metal pattern remains after the exposed photoresist is removed in a process called liftoff, where the metallized diamond is placed in a solvent that effectively lifts off the metal while dissolving photoresist under the metal. In Figure 45, a micrograph of sample *Alpha* is shown after patterning with a 50 nanometers chromium and 750 nanometers of gold.

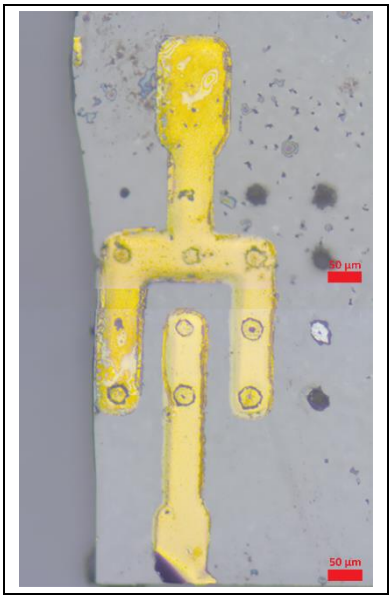

Figure 45: Sample *Alpha* after metallizing with interdigitated readout strips

In order to reduce the leakage current between the interdigitated surface electrodes and the bulk chromium TDVs, sample *Alpha* was annealed at a furnace pressure of 5 Torr in an argon atmosphere at 850°C for ten minutes.

In order to efficiently utilize the diamond as an electrical device, sample *Alpha* was attached to a custom-made PCB which was then housed in an aluminum enclosure with a single 50 Ω impedance Bayonet Neill-Concelman (BNC) bulkhead connections. High voltage is applied through the center pin of the BNC, which is soldered to the PCB pads, to the center electrodes of the interdigitated readout. The outer electrode is held at ground potential through electrical connection to the PCB pad and then the outer sheath of BNC bulkhead connector. 25 μm gold wire is wedge bonded from the pads on the PCB and is Kapton taped onto the diamond surface on either side of the metal readout pattern. Furthermore, the Kapton tape acts to isolate the alpha particle radiation exposure to the active region of the diamond detector as much as possible. A picture of sample *Alpha* electrically and mechanically secured to the PCB board and aluminum box is shown in Figure 46.

In order to measure the resistance of the 3D diamond device, a Keithley 6487 Picoammeter was connected to the BNC plug, and a DC bias was applied from 0 to 100 Volts in 10 Volts increments, followed by the same measurements at a negative polarity. The current was allowed to stabilize at each voltage point for two seconds before recording the data. A least squares fit to the resulting current data was used to calculate the resistance of the diamond in between the TDV metal electrodes. The current-voltage (I-V) characteristics of sample *Alpha* are shown in Figure 47.

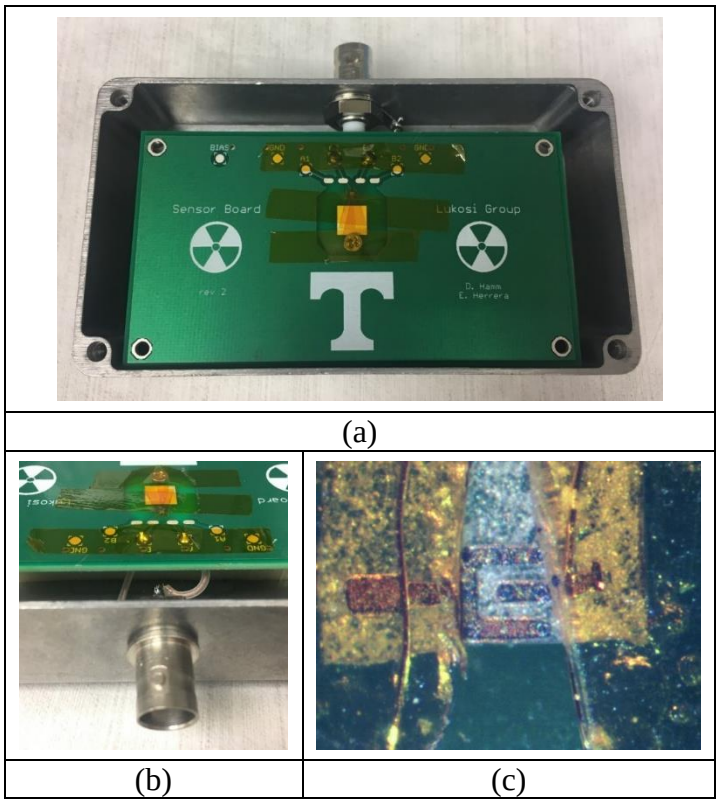

Figure 46: (a) Aluminum enclosure used to house PCB, (b) solder connection points to the bulkhead BNC, and (c) gold wire secured to readout electrodes by Kapton tape

In order to measure the resistance of the 3D diamond device, a Keithley 6487 Picoammeter was connected to the BNC plug, and a DC bias was applied from 0 to 100 Volts in 10 Volts increments, followed by the same measurements at a negative polarity. The current was allowed to stabilize at each voltage point for two seconds before recording the data. A least squares fit to the resulting current data was used to calculate the resistance of the diamond in between the TDV metal electrodes. The current-voltage (I-V) characteristics of sample *Alpha* are shown in Figure 47.

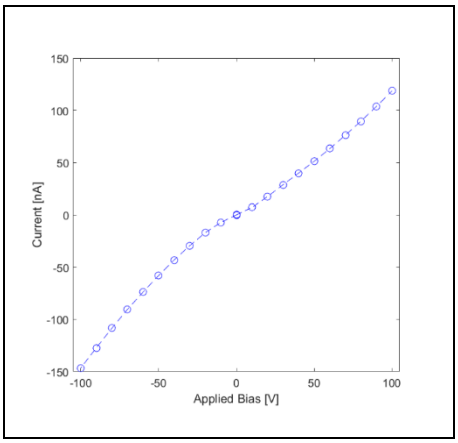

Figure 47: I-V Characteristics of sample Alpha after metallization with the readout pattern

The I-V measurements demonstrated Ohmic behavior characteristic of a properly metallized diamond detector. A resistance of 820 ± 40 MΩ was calculated from the I-V data.

3.5 3D Diamond Detector Response

In order to study the response of sample *Alpha* to ionizing radiation, multiple radioactive sources were utilized. Standard NIM equipment was used to acquire differential pulse height spectra (DPHS) allowing the CCE of the 3D diamond detector to be estimated. During DPHS measurements, a charge sensitive preamplifier (CSA) is connected to the diamond detector. A simplified diagram of a typical CSA is shown in Figure 48.

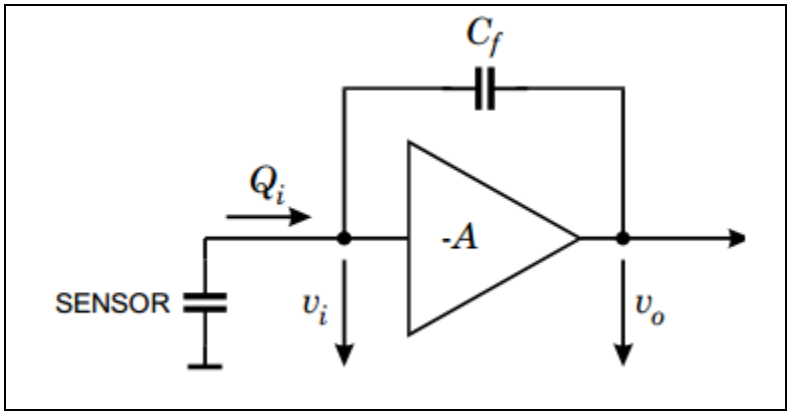

Figure 48: Schematic of a typical CSA used in radiation detection setup [77]

The voltage output of a CSA, v_o, is proportional to the amount of charge induced in the diamond detector Q_i and is expressed as the following:

$$V_{out}(t) \propto Q(t) = \int_0^t i_d \, d\tau \tag{8}$$

Electric charge is created when electron-hole pairs are liberated through ionizing radiation energy interactions. The charges drift in the electric field created by the bias applied to the diamond detector, inducing a pulse of current i_d onto the feedback capacitor C_f of the CSA over the time *t*. A feedback resistor R_f is placed in parallel with the feedback capacitor to reset the output of the CSA. The open-loop gain of the operational amplifier, A, is always very large.

After being amplified by the CSA, the diamond detector signal was directed into an Ortec 572A Shaping Amplifier. Shaping amplifiers provide further gain to the signal, while decreasing high frequency noise through a low-pass filter. In addition, the detector signal can be further tailored by the shaping time of the amplifier. The shaping time is related to the band pass frequency of the amplifier. Thus, selecting a shaping time that minimize electronic noise while collecting that maximum signal is essential to operating a radiation detector properly. Finally, the signal was routed to an Ortec ASPEC-927 Multi-Channel Analyzer (MCA) and analog-to-digital converted (ADC) which was connected to a Windows PC. A diagram of the complete DPHS experiment chain is shown in Figure 49.

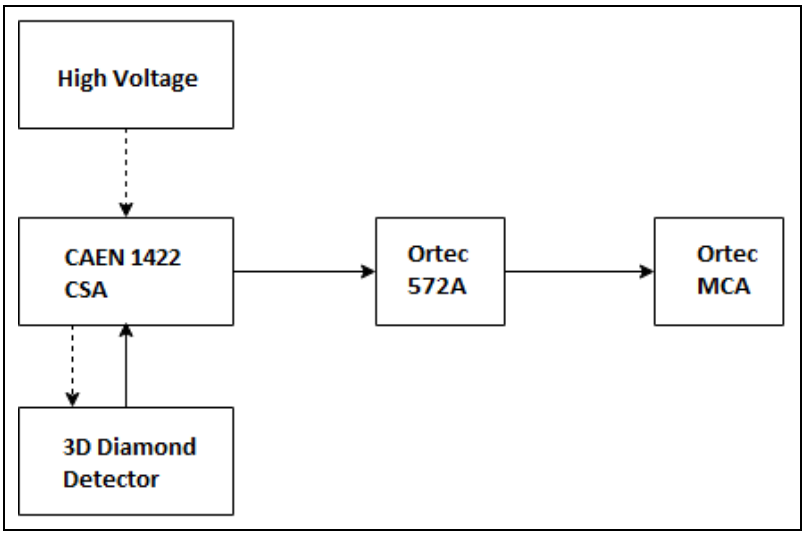

Figure 49: Diagram of DPHS experimental setup chain

3.5.1 Polyenergetic Neutron Source

In order to test the functionality of sample *Alpha* as a 3D radiation detector, it was exposed to an unmoderated, 2 Curie plutonium-beryllium neutron source emitting a broad spectrum of neutron energies from less than 0.15 eV up to 11 MeV [78, 79]. The primary interaction mechanism of neutrons in the diamond detector is elastic scattering, where a carbon nucleus is displaced from its initial lattice site through momentum transferred from the energetic neutron. Inelastic scattering reactions also take place in the diamond detectors when the incident neutron energy is greater than 4.8 MeV [80]. These reactions produce charged alpha particles, which are efficiently detected in the diamond material. An example ^{239}Pu/Be neutron spectrum measured by a planar diamond detector is shown in Figure 50.

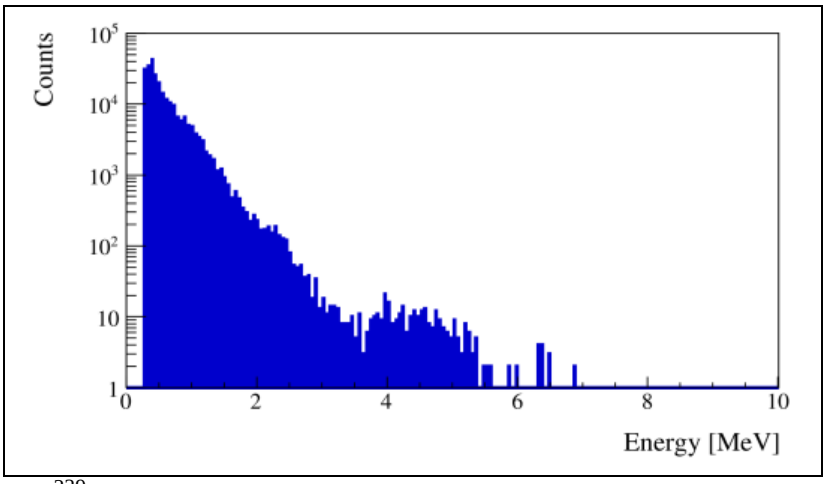

Figure 50: ^{239}Pu/Be neutron source measured by planar diamond detector [81]

Due to the small active detection volume of the detector, the higher energy neutron inelastic scattering interactions were not observed in the spectrum produced by sample *Alpha*. However, elastic neutron scattering reactions above the noise floor are clearly observed at less than 1 MeV and are shown in the DPHS in Figure 51. Using recoiling carbon nuclei produced through neutron elastic scattering reactions, it was shown that sample *Alpha* operated successfully as a 3D diamond radiation detector with TDV metal electrodes.

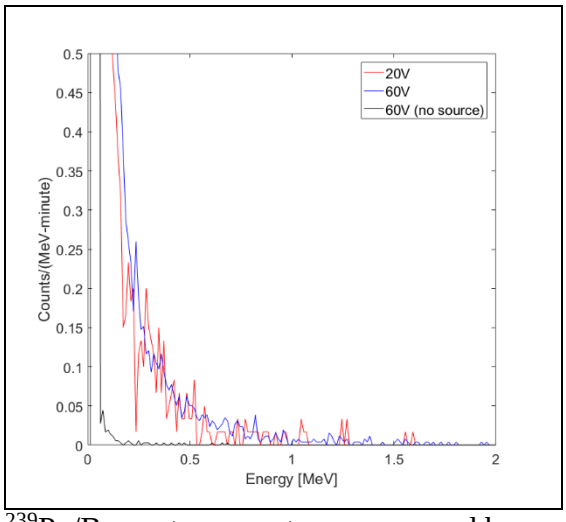

Figure 51: ^{239}Pu/Be neutron spectrum measured by sample *Alpha*

3.5.2 Polyenergetic Alpha Particle Source

The next radiation exposure conducted on sample *Alpha* was using an Americium-241 smoke detector alpha particle source. This source emits beta particles, x-rays, and alpha particles with a myriad of alpha energies ranging from 4.758 to 5.546 MeV, according to the National Nuclear Data Center. However, the probability of emission per decay is less than 0.001% for most of the energies. The most probable alpha particle energies per decay are 5.443 and 5.486 MeV, which occur 13.1% and 84.8% of the time, respectively. The initial activity of the ^{241}Am source used was 1.0 µCi, and the source was placed as close to sample *Alpha* as possible to maximize the count rate and minimize charged particle energy loss in the air. In order to provide an estimation of sample *Alpha*'s CCE, a silicon charge particle detector was utilized to calibrate the system. This was accomplished by biasing the Si detector to full CCE while irradiating the detector with a monoenergetic ^{210}Po alpha particle source, which produces one 5.304 MeV alpha particle for every radioactive decay. DPHS obtained using sample *Alpha* biased at various electric potentials and a comparison of the 30 V spectrum with the Si calibration spectrum are shown in Figure 52.

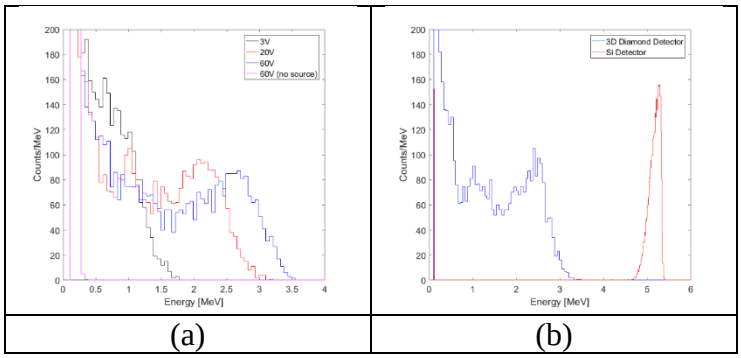

(a) (b)

Figure 52: (a) Electric field-dependent response of sample *Alpha* to Americium-241 polyenergetic alpha particles and (b) comparison of 3D diamond detector (30 V;45% CCE) to Si charged particle detector (200 V;100% CCE). All spectra were obtained with a 2-minute live time.

The peak centroid reached a maximum of 2.86 MeV at a bias of 200 Volts, achieving a CCE of 52.3% when comparing to the average ^{241}Am alpha energy of 5.465 MeV. To estimate the charge carrier mobility-lifetime product, also called the mu-tau product, the applied bias was increased until the amount of charge collected saturated. Then using Equation 1 from Section 1.1.2.1 and a least squares fit, the electron mobility-lifetime product was determined to be $(4.93\pm0.70)\times10^{-6}$ cm^2/V. The low CCE and mu-tau products are hypothesized to be effects of the backside thinning causing microcracking in the diamond bulk. These microcracks decreased the performance of the single crystal diamond to that of a polycrystalline diamond. However, the 3D TDVs clearly increased the amount of charge collected relative to a coplanar diamond detector. Compared to the performance of coplanar diamond detectors with the same electrode spacing of 100 µm reported in the literature, sample *Alpha* achieved a CCE a factor of three higher. In order to study polarization effects within sample *Alpha*, a long exposure of alpha irradiation was conducted over 24 hours with the 3D diamond detector biased the entire time. This DPHS is shown in Figure 53.

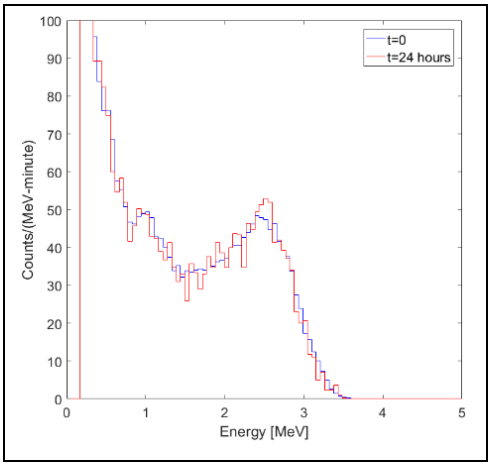

Figure 53: Demonstration of lack of polarization after 24 hours of operating at 45 V

Neither the peak centroid nor the count rate noticeably decreased over the day long measurement.

3.5.3 Cadmium-109 Source

To verify that the 3D diamond detector could operate as an X-ray detector, a sealed ^{109}Cd source with an initial activity of 351 microCuries was utilized as an X-ray and gamma ray source. Figure 54 displays the pulse height spectrum produced by sample *Alpha* when exposed to a ^{109}Cd radioactive source.

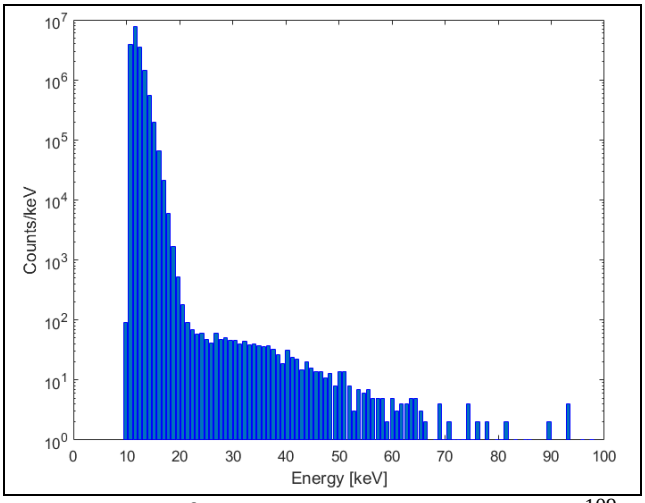

Figure 54: Response of the 3D diamond detector to a ^{109}Cd source

The Compton edge from the 88 keV ^{109}Cd gamma-rays was present at 22 keV. At lesser energies, the sharp increase in counts is due to the much more intense ~22 keV X-rays, where the ratio of Compton scattering to photoelectric effect interactions are roughly equal. The 3D diamond detector performed as expected since the 88 keV gamma rays were only slightly attenuated by the 150 μm thick diamond.

3.5.4 Comparison to Coplanar Diamond Detector

In order to demonstrate that the promising radiation detection response from sample *Alpha* is due to the novel TDV Cr metal electrodes, a detector-grade diamond from Element Six was metallized with the same readout scheme in the same manner as the 3D diamond detector. The sample was boiled in the same basic acid bath as samples *Alpha* and *Beta* to provide a clean surface for patterning, was rinsed in deionized water, and was blown dry with nitrogen gas. A brief (3 minute) oxygen plasma exposure at 100W and 60 mTorr in a PlasmaTherm capacitvely-coupled plasma RIE machine was then used on the diamond sample to further oxidize the surface. A similar Cr/Au stack of metal was applied via photolithography and magnetron sputtering, which was followed by annealing in Argon atmosphere at 5 Torr for 850°C for ten minutes. The sample with the coplanar readout was mounted and wire bonded on a ceramic PCB board, similar to sample *Alpha*. Through vias in the PCB were soldered to a bulkhead BNC connection to provide a connection for the detector bias and output. An aluminum enclosure box was used to house the diamond detector and PCB. A micrograph of the coplanar diamond compared to the 3D diamond with TDVs is shown in Figure 55.

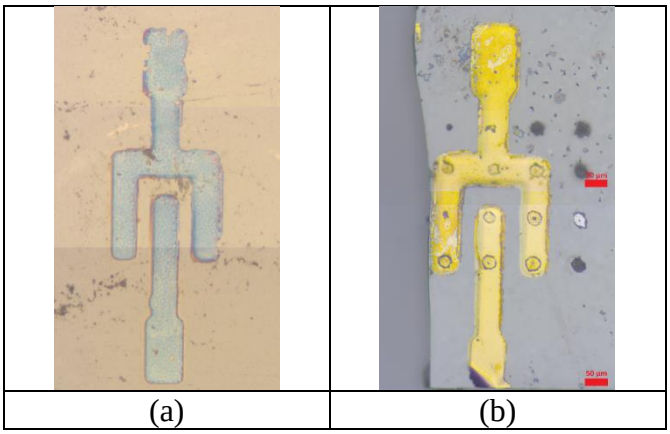

Figure 55: Optical micrograph comparing the (a) planar diamond detector and (b) the 3D diamond detector

The contrasting colors of the metal electrodes were due to sample *Alpha* having a much thicker layer of gold.

The diamond with the coplanar readout was then connected to the exact same electronic equipment as that shown in Figure 49 to provide a direct comparison to the performance of sample *Alpha*. It should be noted that previous research reported in the literature demonstrated that coplanar diamond detectors can detect alpha particles with a CCE dependent on the separation distance of the coplanar electrodes [82, 83]. Furthermore, the studies discussed TCAD simulations that calculated the depth of the electric field profile to be less than the range of the alpha particle, demonstrating a need for improving the electric field profile through penetrating electrodes to obtain higher levels of CCE. The electric field dependent DPHS measurements obtained from the coplanar diamond is shown in Figure 56.

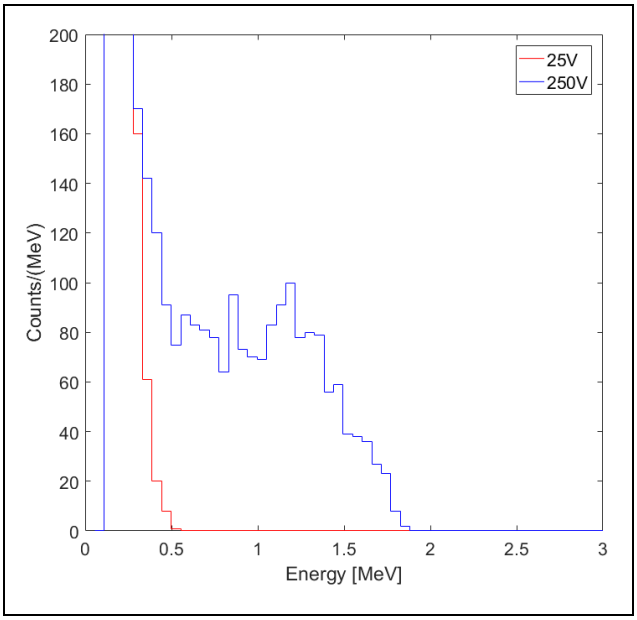

Figure 56: Response of coplanar diamond detector with identical readout to ^{241}Am alpha particles at biases of 25 V and 250 V

The low CCE obtained from the coplanar diamond even at higher bias values agreed with CCE data in the literature. At an applied bias of 250 V, the coplanar diamond detector achieved a CCE of only 22.3%. The electric field does not penetrate as deep as the alpha particles traverse. It was evident that the electric field of sample *Alpha* penetrated much deeper into the diamond surface, due to the propagation of the applied bias and associated electric field through the diamond bulk. A comparison of the DPHS obtained from sample *Alpha* and the coplanar diamond is shown in Figure 57.

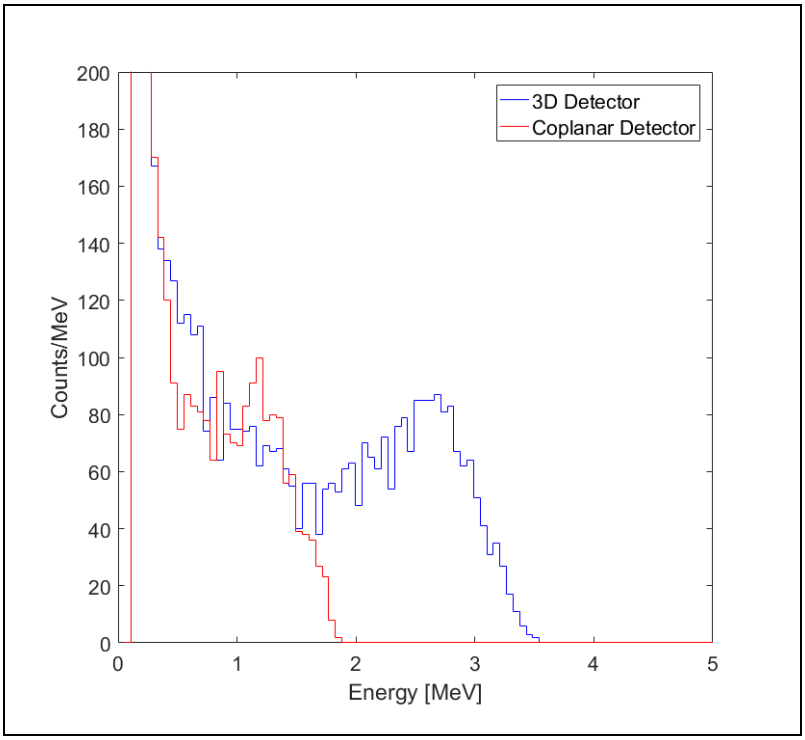

Figure 57: Comparison of 3D diamond detector (60 V;47.6% CCE) and coplanar diamond detector (250 V; 22.3% CCE)

The last property of the 3D diamond detector, sample *Alpha*, that was investigated was the resistivity of the chromium TDV metal electrodes. A thin layer (~100 nm) of chromium metal was sputtered onto the surface of the backside of sample *Alpha*. The detector was then

placed onto silver epoxy on a microscope slide to establish electrical contact with the vias on the backside of the diamond. Examination of the front side of the diamond was made possible by utilizing an electrical characterization probe station with a microscope. Electrical contact to the TDVs and the silver epoxy was made using tungsten probe tips attached to micromanipulators. A DC electrical potential from zero to 300 mV was applied in increments of 25 mV to the tungsten probe tips using a Keithely 6487 Picoammeter. A micrograph of sample *Alpha*, the tungsten probe tips, and the silver epoxy is shown in Figure 58, in addition to the acquired I-V curve.

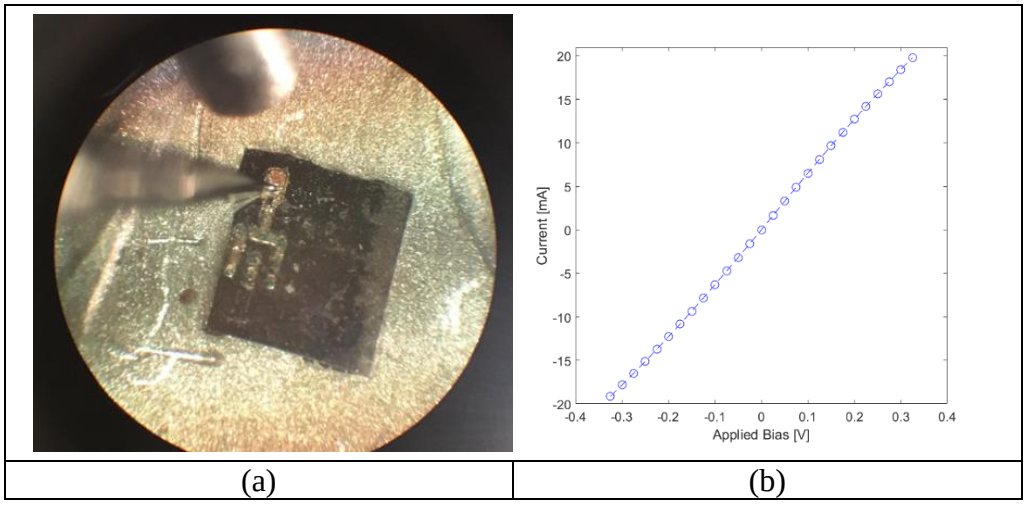

(a) (b)

Figure 58: (a) Micrograph of 3D diamond detector during TDV I-V measurements and (b) resulting I-V curve

A least squares fit to the I-V curve determined that the resistance of the TDVs were 61.4 ± 0.6 mΩ. Using the known diameter and thickness of the chromium-filled TDVs, the average resistivity of the TDVs was calculated to be $(2.89\pm0.03)\times10^{-5}$ Ω-cm.

3.9 Conclusions

A novel fabrication process for creating TDVs was demonstrated in one optical-grade diamond and one electronic-grade diamond. The TDVs had aspect ratios of 1.0 and 5.0, respectively, and were created by oxygen and argon plasma DRIE of the diamond substrate, which was masked with a SS foil. EDM had been used to machine a 4x4 grid of 70 µm and 30 µm diameter holes in the foil spaced 500 µm and 100 µm apart for the optical and electronic-grade diamonds, respectively. Once the TDVs extended the full thickness of the diamond, chromium electroplating was utilized to fill the holes with a conductive material to create electrodes. An interdigitated strip pattern was metallized on the electronic-grade diamond's surface to connect the plated TDVs. The device was mounted on a PCB in an aluminum enclosure box and was connected to standard NIM equipment. Alpha and neutron irradiation of the diamond demonstrated successful device performance of the first-of-a-kind device. A maximum CCE of 52.3% was achieved during alpha particle detection. Furthermore, the device's performance was directly compared to coplanar diamond detector with an identical metallization scheme. The 3D diamond with electroplated chromium TDVs demonstrated a factor of three higher CCE than the coplanar diamond detector, exhibiting for the first time a 3D diamond detector with fully penetrating metal electrodes. The resistivity of the TDVs was calculated to be $(2.89\pm0.03)\times10^{-5}$ Ω-cm.

Chapter 4: Spatial Response of KSr_2I_5:Eu 2% Scintillating Crystals to Collimated Ionizing Radiation

Summary

A relatively new scintillation crystal composed of potassium strontium iodide activated with europium has been explored as a photon radiation detector. KSr_2I_5:Eu 4% crystals have an excellent energy resolution of 2.4% at 662 keV, a high light yield of around 94,000 photons/MeV, and demonstrate great proportionality over the energy range of 14 to 1275 keV [84]. The crystals were grown using the Bridgman technique with a pulling rate of 1 millimeter per hour and were cooled at a rate of 5°C per hour. A picture of the KSr_2I_5:Eu crystal boule is shown in Figure 59.

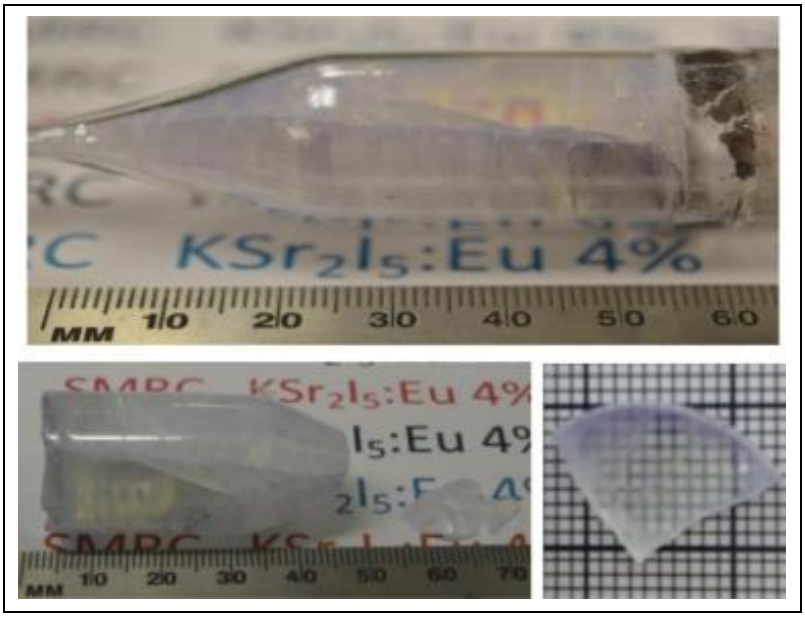

Figure 59: As-grown boule of KSr2I5:Eu 4% and 1x1 cm cross-sectional piece

The crystals were optically transparent after polishing and were sectioned using a diamond wire saw. Packaging of a 2.4 cm diameter by 2.1 cm tall KSr_2I_5:Eu 2% cylinder was conducted by Agile. A picture of the packaged crystal is shown in Figure 60.

Figure 60: Packaged KSr_2I_5:Eu crystal

While the scintillation properties of this crystal are promising for gamma ray spectroscopy, the KSr_2I_5:Eu crystals emit internal background radiation due to the presence of ^{40}K, which could restrict the sensitivity during low-level activity isotope identification. The internal background spectrum in KSr_2I_5:Eu is that of potassium-40, which has a continuous beta particle energy spectrum from 560 to 1311 keV emitted 89% of the time and 1461 keV gamma ray emitted 11% of the time. Effects of internal background radiation on KSr_2I_2:Eu crystal have been investigated by Rust *et al.* [85]. The measured and simulated internal background spectrum and a ^{137}Cs differential pulse height spectrum exhibiting excellent energy resolution [86] are shown in Figure 61.

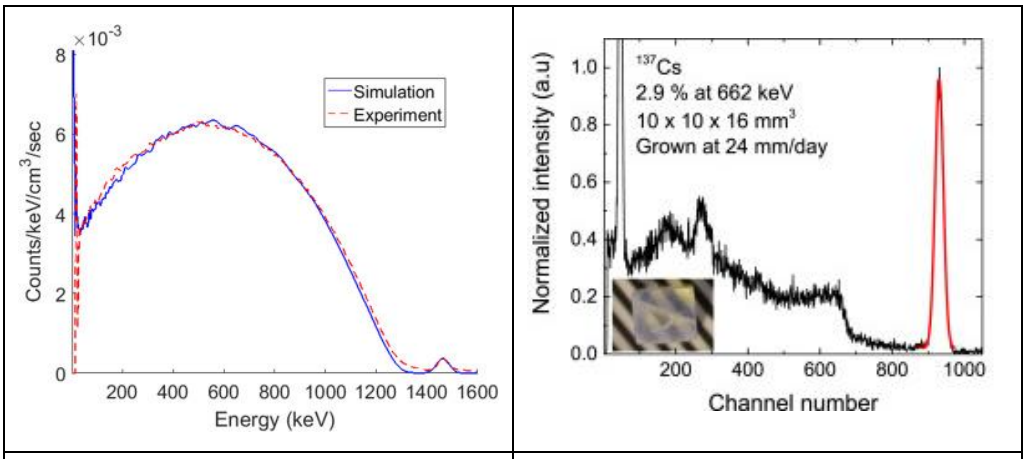

(a) (b)

Figure 61: Differential pulse height spectra of (a) internal background radiation [85] and (b) ^{137}Cs [86]

In order to determine the percentage of high energy photons stopped and the average depth of penetration of X-rays in the crystal, the total mass attenuation coefficient of KSr_2I_5:Eu was calculated. This was accomplished by utilizing the NIST Mass Attenuation Coefficient database to find the mass attenuation coefficient for the constituent compounds at various photon energies. The total mass attenuation coefficient was then calculated using the following relationship:

$$\frac{\mu}{\rho} = \sum_i w_i \left(\frac{\mu}{\rho}\right)_i \tag{8}$$

where w_i is the weight fraction of the i^{th} element and $\left(\frac{\mu}{\rho}\right)_i$ is the mass attenuation coefficient of the i^{th} element. The mass attenuation coefficient of KSr_2I_5:Eu as a function of photon energy is shown in Figure 62.

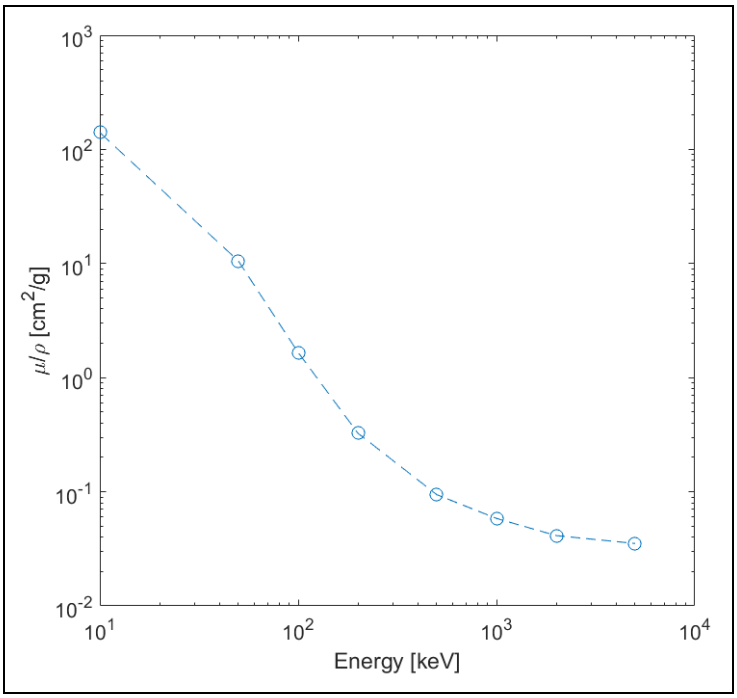

Figure 62: Mass attenuation coefficient of KSr2I5 4% Eu as a function of photon energy

In order examine the uniformity of the scintillator detector response, 88 keV X-rays were collimated to a spot size of 3.0 mm and were rastered across the entire packaged crystal by moving the Hamamatsu R6231-100 photomultiplier tube (PMT) and KSr_2I_5:Eu crystal inside a dark box. The 2-inch-long collimator was constructed by stacking four blocks of SS that were each 0.5 inches thick, 1.5 inches in width and length, and contained a 2.0 mm hole in the center. A sealed Cadmium-109 source with an initial activity of 482 microCuries was used as the interrogating photon source. The ^{109}Cd source was a 1-inch diameter button source with the radioactive material located in the center 3 mm of the disc. The source was aligned with the collimation aperture and was attached to the collimator using Kapton tape. In order to reduce the count rate from scattered X-rays, 9 mm of lead was placed behind, on top, and in front of the collimator, which was resting on a 2-inch thick lead brick. The sheet in front of the collimator

contained a 3.0 mm hole for collimated X-rays to pass through. A picture of the KSr_2I_5:Eu crystal, SS collimator, and lead shielding inside of the dark box is shown in Figure 63.

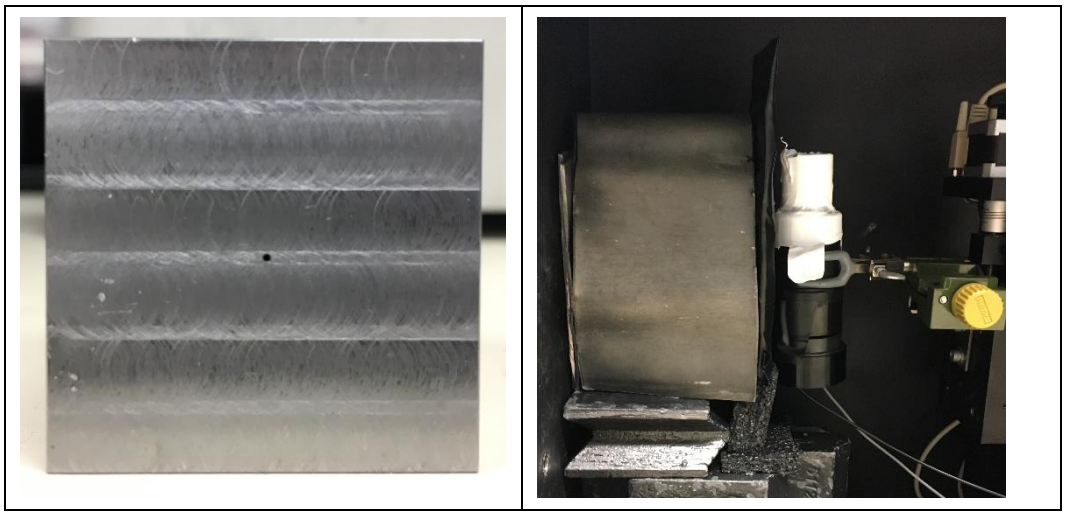

Figure 63: Photograph of the SS collimator, lead shielding, and KSr2I5:Eu crystal in the detector dark box

Using the linear attenuation coefficient μ, it was calculated that 99% of the 88 keV X-Rays were stopped in the first 2.8 mm of KSr_2I_5:Eu, allowing for near surface probing of the crystal's scintillation properties.

At the time of measurements, the total activity of the 482 µCi cadmium-109 source had been reduced to 351 µCi through radioactive decay. 88 keV photons are only emitted 3.644% of the time, reducing the effective 88 keV emission rate to 12.8 µCi or 473,000 photons per second. The count rate of 88 keV photons detected by the crystal was further reduced to about 3 counts per second by the size of the collimator aperture and the small solid angle induced by the relatively large source-to-detector distance. In order to measure at least 1000 counts in the 88 keV photopeak, a count time of ten minutes was used for each data point in the spatial response program. With the crystal diameter of 24 mm, height of 21 mm, and effective spot size of 3 mm,

a grid of 8x8 scans was conducted to maximize the spatial resolution. A Matlab post-processing script was written to read and analyze the data and to plot the spatial response data as a function of crystal height and width. An example DPHS produced by KSr_2I_5:Eu when exposed to the collimated ^{109}Cd source is shown in Figure 64.

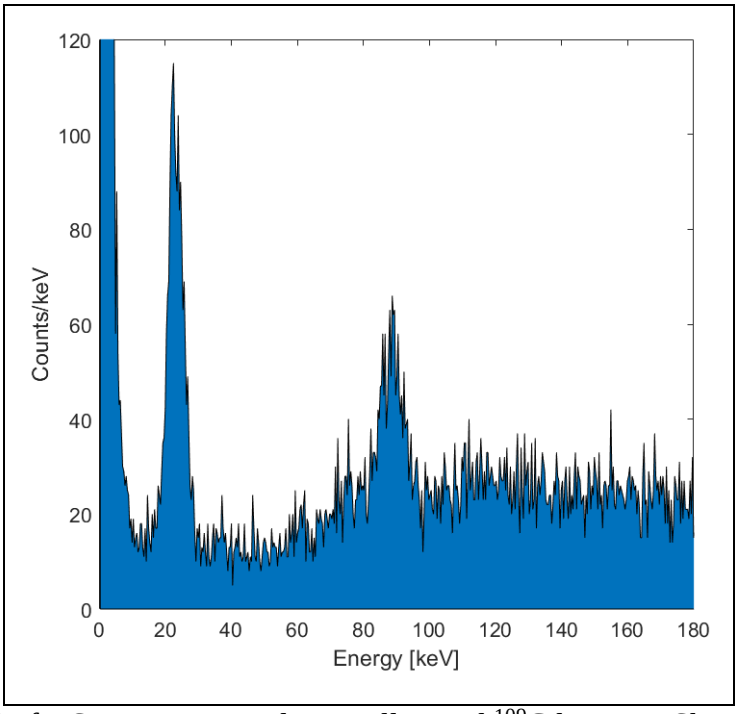

Figure 64: DPHS of KSr_2I_5:Eu exposed to a collimated ^{109}Cd source; Shaping time of 10 µs

The spatial response of a KSr_2I_5:Eu crystal with regards to peak centroid bin number and energy resolution at 88 keV is shown in Figure 65. The centroid bin number had an average of 247.2 ± 2.6, while the energy resolution had an average of 8.82 ± 0.74%. A packaged 2.54 cm diameter and 2.54 inch tall SrI_2:Eu scintillation crystal from CapeSym Technologies was scanned with the system to compare to the KSr_2I_5:Eu. Figure 66 shows the spatial response of a packaged SrI_2:Eu crystal.

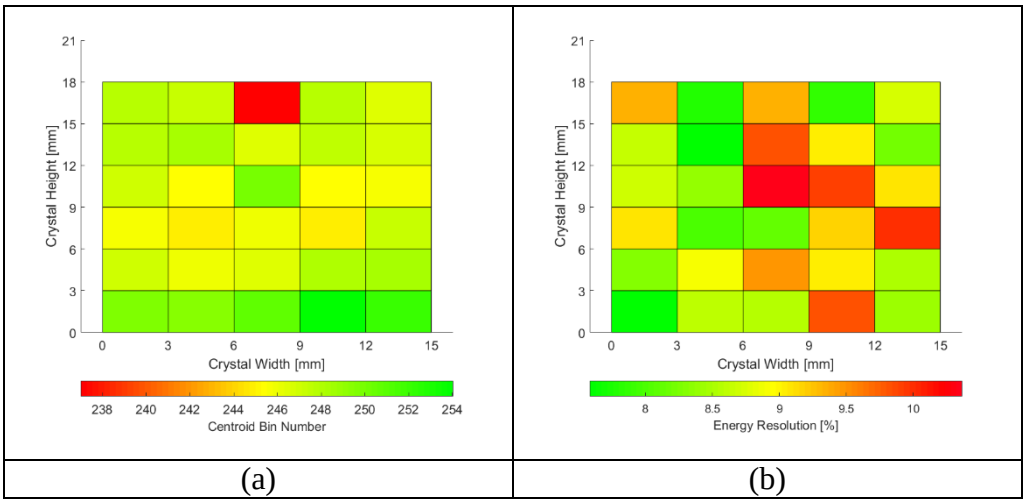

(a) (b)

Figure 65: Spatial response of KSr_2I_5:Eu with regards to (a) centroid bin number and (b) energy resolution

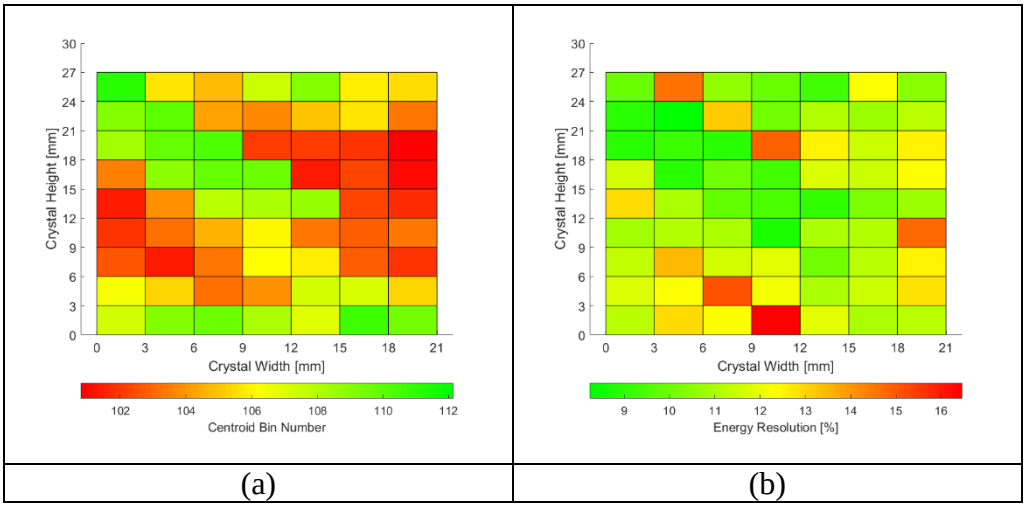

(a) (b)

Figure 66: Spatial response of SrI_2:Eu with regards to (a) centroid bin number and (b) energy resolution

The centroid bin number had an average of 105.8 ± 3.2, while the energy resolution had an average of 11.2 ± 1.6%. It should be noted that the gain on the shaping amplifier was decreased by a factor a 2.5 to account for the increased brightness and associated dead time of the SrI_2:Eu crystal. The results of the spatial response mapping indicate that KSr_2I_5:Eu had more uniform scintillation response and a better energy resolution than SrI_2:Eu at 88 keV.

References

1. de Boer, W., et al., *Radiation hardness of diamond and silicon sensors compared.* physica status solidi (a), 2007. **204**(9): p. 3004-3010.
2. Balmer, R., et al., *Chemical vapour deposition synthetic diamond: materials, technology and applications.* Journal of Physics: Condensed Matter, 2009. **21**(36): p. 364221.
3. Tsung, J.W., et al., *Signal and noise of diamond pixel detectors at high radiation fluences.* Journal of Instrumentation, 2012. **7**(09): p. P09009.
4. Affolder, A., P. Allport, and G. Casse, *Charge Collection Efficiency Measurements of Heavily Irradiated Segmented n-in-p and p-in-n Silicon Detectors for Use at the Super-LHC.* IEEE Transactions on Nuclear Science, 2009. **56**(3): p. 765-770.
5. Casse, G., et al., *Enhanced efficiency of segmented silicon detectors of different thicknesses after proton irradiations up to 1× 10 16 n eq cm 2.* Nuclear Instruments and Methods in Physics Research Section A: Accelerators, Spectrometers, Detectors and Associated Equipment, 2010. **624**(2): p. 401-404.
6. Pietraszko, J., et al., *Radiation damage in single crystal CVD diamond material investigated with a high current relativistic 197Au beam.* Nuclear Instruments and Methods in Physics Research Section A: Accelerators, Spectrometers, Detectors and Associated Equipment, 2014. **763**: p. 1-5.
7. Bentele, B., et al., *Rate dependence, polarization, and light sensitivity of neutron-irradiated scCVD diamond sensors.* Nuclear Instruments and Methods in Physics Research Section A: Accelerators, Spectrometers, Detectors and Associated Equipment, 2016. **838**: p. 74-81.
8. Urlau, R.R., H.J. Logie, and F.R.N. Nabarro, *Energy Levels in the Forbidden Gap of Insulating Diamonds.* Proceedings of the Physical Society, 1961. **78**(2): p. 256.
9. Willardson, R.K. and G.C. Danielson, *Effect of Light on a Diamond Conduction Counter.* Physical Review, 1950. **77**(2): p. 300-301.
10. Pernegger, H., *High mobility diamonds and particle detectors.* physica status solidi (a), 2006. **203**(13): p. 3299-3314.
11. Manfredotti, C., F. Fizzotti, and Y. Garino, *The primed state of CVD diamond under blue light illumination.* Diamond and Related Materials, 2006. **15**(9): p. 1362-1368.
12. Manfredotti, C., et al., *Effects of light on the 'primed' state of CVD diamond nuclear detectors.* Diamond and Related Materials, 2002. **11**(3–6): p. 446-450.
13. Guthoff, M., et al., *Radiation damage in the diamond based beam condition monitors of the CMS experiment at the Large Hadron Collider (LHC) at CERN.* Nuclear Instruments and Methods in Physics Research Section A: Accelerators, Spectrometers, Detectors and Associated Equipment, 2013. **730**: p. 168-173.
14. Canali, C., et al., *Electrical properties and performances of natural diamond nuclear radiation detectors.* Nuclear Instruments and Methods, 1979. **160**(1): p. 73-77.
15. Kozlov, S., et al., *Preparation and characteristics of natural diamond nuclear radiation detectors.* Nuclear Science, IEEE Transactions on, 1975. **22**(1): p. 160-170.
16. Kramberger, G., *Signal development in irradiated silicon detectors*. 2001, Stefan Inst., Ljubljana.
17. Ziegler, J.F., M.D. Ziegler, and J.P. Biersack, *SRIM – The stopping and range of ions in matter (2010).* Nuclear Instruments and Methods in Physics Research Section B: Beam Interactions with Materials and Atoms, 2010. **268**(11–12): p. 1818-1823.

18. Li, Z. and H.W. Kraner, *Modeling and simulation of charge collection properties for neutron irradiated silicon detectors.* Nuclear Physics B - Proceedings Supplements, 1993. **32**(0): p. 398-409.
19. Eaton-Magaña, S. and C.M. Breeding, *AN INTRODUCTION TO PHOTOLUMINESCENCE SPECTROSCOPY FOR DIAMOND AND ITS APPLICATIONS IN GEMOLOGY.* Gems & Gemology, 2016. **52**(1): p. 2-17.
20. Shockley, W. and W. Read Jr, *Statistics of the recombinations of holes and electrons.* Physical review, 1952. **87**(5): p. 835.
21. Sobolev E V, I.i.V.E., and Yur'eva O P, Sov. Phys.-Solid St, 1969. **11**: p. 938-43.
22. Shigley, J.E. and C.M. Breeding, *OPTICAL DEFECTS IN DIAMOND: A QUICK REFERENCE CHART.* Gems & Gemology, 2013. **49**(2).
23. Balmer, R., et al., *Unlocking diamond's potential as an electronic material.* Philosophical Transactions of the Royal Society of London A: Mathematical, Physical and Engineering Sciences, 2008. **366**(1863): p. 251-265.
24. Zaitsev, A., et al., *Handbook of Industrial Diamonds and Diamond Films.* Prelas, M, 1998: p. 227-376.
25. Sussmann, R.S., *CVD diamond for electronic devices and sensors*. Vol. 26. 2009: John Wiley & Sons.
26. Konov, V.I., *Laser in micro and nanoprocessing of diamond materials.* Laser & Photonics Reviews, 2012. **6**(6): p. 739-766.
27. Pimenov, S., et al., *Laser polishing of diamond plates.* Applied Physics A, 1999. **69**(1): p. 81-88.
28. Wu, Q., et al., *Femtosecond laser-induced periodic surface structure on diamond film.* Applied Physics Letters, 2003. **82**(11): p. 1703-1705.
29. Wang, C., et al., *Laser-induced graphitization on a diamond (111) surface.* Physical review letters, 2000. **85**(19): p. 4092.
30. Preuss, S. and M. Stuke, *Subpicosecond ultraviolet laser ablation of diamond: Nonlinear properties at 248 nm and time-resolved characterization of ablation dynamics.* Applied physics letters, 1995. **67**(3): p. 338-340.
31. Rothschild, M., C. Arnone, and D. Ehrlich, *Excimer-laser etching of diamond and hard carbon films by direct writing and optical projection.* Journal of Vacuum Science & Technology B: Microelectronics Processing and Phenomena, 1986. **4**(1): p. 310-314.
32. Rebello, J., D. Straub, and V. Subramaniam, *Diamond growth from a CO/CH4 mixture by laser excitation of CO: Laser excited chemical vapor deposition.* Journal of applied physics, 1992. **72**(3): p. 1133-1136.
33. Kononenko, V.V., et al. *Laser shaping of diamond for IR diffractive optical elements*. in *Second International Symposium on Laser Precision Micromachining*. 2002. International Society for Optics and Photonics.
34. Pavelyev, V., et al., *Diffractive Microoptics for Technological IR-Lasers.* High-Power and Femtosecond Lasers: Properties, Materials and Applications.–Ed. by Paul-Henri Barret and Michael Palmer.–Nova Science Publishers, Inc, 2009: p. 125-158.
35. Pavelyev, V.S., et al. *Diamond DOEs for focusing IR laser beams into pregiven focal domains*. in *Optical Science and Technology, SPIE's 48th Annual Meeting*. 2004. International Society for Optics and Photonics.
36. Kononenko, T., et al., *Femtosecond laser microstructuring in the bulk of diamond.* Diamond and related materials, 2009. **18**(2): p. 196-199.

37. Kononenko, T., et al., *All-carbon detector with buried graphite pillars in CVD diamond.* Applied Physics A, 2014. **114**(2): p. 297-300.
38. Neff, M., et al., *Femtosecond laser writing of buried graphitic structures in bulk diamond.* Applied Physics A, 2009. **97**(3): p. 543.
39. Strekalov, V., et al., *Early stages of laser graphitization of diamond.* Applied Physics A: Materials Science & Processing, 2003. **76**(4): p. 603-607.
40. Lagomarsino, S., et al., *Three-dimensional diamond detectors: Charge collection efficiency of graphitic electrodes.* Applied Physics Letters, 2013. **103**(23): p. 233507.
41. Lagomarsino, S., et al., *Electrical and Raman-imaging characterization of laser-made electrodes for 3D diamond detectors.* Diamond and Related Materials, 2014. **43**: p. 23-28.
42. Shimizu, M., et al., *Periodic metallo-dielectric structure in diamond.* Optics express, 2009. **17**(1): p. 46-54.
43. Oh, A., et al., *A novel detector with graphitic electrodes in CVD diamond.* Diamond and Related Materials, 2013. **38**: p. 9-13.
44. William, S., *Semiconductive wafer and method of making the same*. 1962, Google Patents.
45. Smith, M.G. and S. Emanuel, *Methods of making thru-connections in semiconductor wafers*. 1967, Google Patents.
46. Filik, J., *Raman spectroscopy: a simple, non-destructive way to characterise diamond and diamond-like materials.* Spectroscopy Europe, 2005. **17**(5): p. 10.
47. Ding, G., et al., *Micromachining of CVD diamond by RIE for MEMS applications.* Diamond and related materials, 2005. **14**(9): p. 1543-1548.
48. Forsberg, P. and M. Karlsson, *High aspect ratio optical gratings in diamond.* Diamond and Related Materials, 2013. **34**: p. 19-24.
49. Hausmann, B.J., et al., *Fabrication of diamond nanowires for quantum information processing applications.* Diamond and Related Materials, 2010. **19**(5): p. 621-629.
50. Otterbach, R. and U. Hilleringmann, *Reactive ion etching of CVD-diamond for piezoresistive pressure sensors.* Diamond and related materials, 2002. **11**(3): p. 841-844.
51. Chapman, B.N., *Glow discharge processes*. 1980: Wiley.
52. Instruments, O., *Plasmalab System 100*, O.I.P.S. 100, Editor. 2015, Oxford Instruments: http://www.oxfordplasma.de/.
53. Williams, P., *Plasma processing of semiconductors*. Vol. 336. 2013: Springer Science & Business Media.
54. Holland, L., *Some characteristics and uses of low-pressure plasmas in materials science.* Journal of Vacuum Science and Technology, 1977. **14**(1): p. 5-15.
55. Holland, L. and S. Ojha, *The chemical sputtering of graphite in an oxygen plasma.* Vacuum, 1976. **26**(2): p. 53-60.
56. Coburn, J. and H.F. Winters, *Ion-and electron-assisted gas-surface chemistry—An important effect in plasma etching.* Journal of Applied physics, 1979. **50**(5): p. 3189-3196.
57. Laermer, F. and A. Schilp, *Method of anisotropically etching silicon*. 1996, Google Patents.
58. Wikipedia. *Deep reactive-ion etching*. 2017 [cited 2017 March 13]; Available from: https://en.wikipedia.org/wiki/Deep_reactive-ion_etching.

59. Henry, M.D., et al., *Alumina etch masks for fabrication of high-aspect-ratio silicon micropillars and nanopillars.* Nanotechnology, 2009. **20**(25): p. 255305.
60. Niedermann, P., et al., *CVD diamond probes for nanotechnology.* applied physics a: materials science & processing, 1998. **66**: p. S31-S34.
61. Shibata, T., et al., *Micromachining of diamond film for MEMS applications.* Journal of microelectromechanical systems, 2000. **9**(1): p. 47-51.
62. Forneris, J., et al., *A 3-dimensional interdigitated electrode geometry for the enhancement of charge collection efficiency in diamond detectors.* EPL (Europhysics Letters), 2014. **108**(1): p. 18001.
63. Walkup, R.E., K.L. Saenger, and G.S. Selwyn, *Studies of atomic oxygen in O2+CF4 rf discharges by two-photon laser-induced fluorescence and optical emission spectroscopy.* The Journal of Chemical Physics, 1986. **84**(5): p. 2668-2674.
64. Vargas Catalan, E., et al., *Controlling the profile of high aspect ratio gratings in diamond.* Diamond and Related Materials, 2016. **63**: p. 60-68.
65. Hwang, D., T. Saito, and N. Fujimori, *New etching process for device fabrication using diamond.* Diamond and Related Materials, 2004. **13**(11): p. 2207-2210.
66. Ando, Y., et al., *Smooth and high-rate reactive ion etching of diamond.* Diamond and Related Materials, 2002. **11**(3–6): p. 824-827.
67. Tran, D.T., *Investigation of diamond etching by a microwave plasma-assisted system*. 2010, Michigan State University.
68. Dorsch, O., M. Werner, and E. Obermeier, *Dry etching of undoped and boron doped polycrystalline diamond films.* Diamond and Related Materials, 1995. **4**(4): p. 456-459.
69. Le, T.S., et al., *Effect of coating and plasma treatments on the induced coupled plasma-reactive ionic etching of boron-doped diamond for microelectromechanical systems (MEMS) applications.* Nanoscience Methods, 2014. **3**(1): p. 1-10.
70. Sandhu, G. and W. Chu, *Reactive ion etching of diamond.* Applied physics letters, 1989. **55**(5): p. 437-438.
71. Yunata, E.E. and T. Aizawa, *Micro-grooving into thick CVD diamond films via hollow-cathode oxygen plasma etching.* Manufacturing Letters, 2016. **8**: p. 16-20.
72. Bachmair, F., et al., *A 3D diamond detector for particle tracking.* Nuclear Instruments and Methods in Physics Research Section A: Accelerators, Spectrometers, Detectors and Associated Equipment, 2015. **786**: p. 97-104.
73. Lagomarsino, S., et al., *Radiation hardness of three-dimensional polycrystalline diamond detectors.* Applied Physics Letters, 2015. **106**(19): p. 193509.
74. Galbiati, A., et al., *Performance of monocrystalline diamond radiation detectors fabricated using TiW, Cr/Au and a novel ohmic DLC/Pt/Au electrical contact.* IEEE Transactions on Nuclear Science, 2009. **56**(4): p. 1863-1874.
75. Collins, A., E. Lightowlers, and A. Williams, *Formation of electrical contacts on insulating and semiconducting diamonds.* Diamond Res., 1970: p. 19-22.
76. G, F.C., *Process of electrodepositing chromium and of preparing baths therefor*. 1926, Google Patents.
77. Spieler, H., L. Villaseñor, and V. Villanueva. *Front-End Electronics and Signal Processing*. in *AIP Conference Proceedings*. 2003. AIP.
78. Anderson, M.E. and W.H. Bond, *Neutron spectrum of a plutonium-beryllium source.* Nuclear Physics, 1963. **43**: p. 330-338.

79. Kumar, A. and P.S. Nagarajan, *Neutron spectra of 239PuBe neutron sources.* Nuclear Instruments and Methods, 1977. **140**(1): p. 175-179.
80. Pillon, M., M. Angelone, and A.V. Krasilnikov, *14 MeV neutron spectra measurements with 4% energy resolution using a type IIa diamond detector.* Nuclear Instruments and Methods in Physics Research Section B: Beam Interactions with Materials and Atoms, 1995. **101**(4): p. 473-483.
81. Kavrigin, P., *The spectrum of the PuBe neutron source as measured by a diamond detector with a Cx spectroscopic amplifier.* 2015. p. PuBe neutron source measured spectrum.
82. Galbiati, A., et al., *Characterisation of a coplanar CVD diamond radiation detector.* Nuclear Instruments and Methods in Physics Research Section A: Accelerators, Spectrometers, Detectors and Associated Equipment, 2001. **466**(1): p. 52-57.
83. Wang, S.G., et al., *Diamond-based alpha particle detectors with coplanar geometry.* Diamond and Related Materials, 2003. **12**(3–7): p. 682-686.
84. Stand, L., et al., *Growth and characterization of potassium strontium iodide: A new high light yield scintillator with 2.4% energy resolution.* Nuclear Instruments and Methods in Physics Research Section A: Accelerators, Spectrometers, Detectors and Associated Equipment, 2015. **780**: p. 40-44.
85. Rust, M., C. Melcher, and E. Lukosi, *Intrinsic radioactivity of KSr2I5:Eu2+*. Nuclear Instruments and Methods in Physics Research Section A: Accelerators, Spectrometers, Detectors and Associated Equipment, 2016. **833**: p. 33-37.
86. Stand, L., et al., *Exploring growth conditions and Eu2+ concentration effects for KSr2I5:Eu scintillator crystals.* Journal of Crystal Growth, 2016. **439**: p. 93-98.

Vita

Thomas Gregory Wulz was born on February 16, 1990 in Woodstock, GA to Jeffrey Stephen Wulz and Lee Ann Stabler. Thomas grew up in Atlanta, GA until he was five years old, at which point his family relocated to Cleveland, TN. Later in life, he attended Walker Valley High School where he graduated with honors. Upon graduation from high school in 2008, Thomas moved to Knoxville, TN to pursue a Bachelor's of Science degree in Nuclear Engineering at the University of Tennessee at Knoxville. In 2012, Thomas completed a Nuclear Engineering internship with Tennessee Valley Authority in Chattanooga, TN where he gained practical experience in project management in licensing a proposed nuclear power plant construction project. Thomas returned to UTK to graduate cum laude in May 2013, at which point he began his coursework to obtain a Master's of Science degree in Nuclear Engineering. During graduate school, Thomas worked as a Graduate Research Assistant for Dr. Eric Lukosi, where he began honing his skills and interests in vacuum technology and thin film sciences. His Master's research project consisted of designing, constructing, and operating a chemical vapor deposition system to grown boron carbide films onto silicon substrates. A year later, he graduated with his Master's and made the decision to continue his education at UTK to obtain a PhD. Thomas's doctoral work focused on the development of a novel fabrication process to create full metal electrodes in 3D diamond radiation detectors. He completed his Doctorate of Philosophy degree in May 2017.